Geochemistry 82 (2022) 125860

Contents lists available at ScienceDirect

Geochemistry

journal homepage: www.elsevier.com/locate/chemer

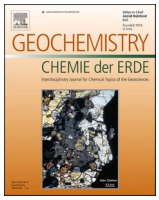

Rodingites from the Veria-Naousa ophiolite (Greece): Mineralogical evolution, metasomatism and petrogenetic processes

Aikaterini Rogkala [a,*], Petros Petrounias [a], Petros Koutsovitis [a], Panagiota P. Giannakopoulou [a], Panagiotis Pomonis [b], Paraskevi Lampropoulou [a], Konstantin Hatzipanagiotou [a]

[a] Department of Geology, Section of Earth Materials, University of Patras, 26504 Patras, Greece
[b] Department of Geology and Geoenvironment, National and Kapodistrian University of Athens, Panepistimioupolis Zografou, 15784 Athens, Greece

ARTICLE INFO

Handling Editor: Wentao Cao

Keywords:
Veria-Naousa ophiolite
Rodingites
Metasomatic fluids
Subduction zone

ABSTRACT

In the Veria-Naousa ophiolitic complex (north Greece), rodingite appears mainly in the form of cross cutting dykes within serpentinised peridotites. It is distinguished into three types, based upon the provenance of its protoliths, textural characteristics, mineralogical assemblages and geochemical affinities. Type I rodigites were derived from boninitic diabasic protoliths and their mineralogical assemblage include garnet + clinopyroxene + chlorite. Type II rodingites were formed at the expense of gabbroic precursors, comprising clinopyroxene + garnet + vesuvianite ± quartz, whereas Type III rodingites replaced diabasic tholeiitic protoliths comprising of garnets + vesuvianite + clinopyroxene + chlorite. Rodingitisation resulted in desilification, decrease of alkalies, Al, Fe, Mg and increase in Ca contents. In Type I rodingites the MREE (middle rare earth elements) and HREE (heavy rare earth elements) were slightly reduced. Type II rodingites experienced LREE (light rare earth elements) depletions, whereas MREE and HREE remained fairly stable. Restricted mobility of REE in Type III rodingites is assigned to shallow-level rodingitisation under decreasing pH.

Rodingitisation occured in two distinct stages at fore-arc settings. The first stage occured under mildly oxidising conditions and enhanced CO_2/H_2O ratios. This stage affected the protoliths of all rodingite types. The second rodingitisation stage occured under more oxidising conditions and lower CO_2/H_2O ratios, which corresponds to the exhumation stage of the serpentinite-rodingite formations. Types II and III rodingites were subjected to further rodingitisation under the increasing influence of slab-derived hydrous phases at shallower depths, leading to the formation of late-stage andradite and vesuvianite. All stages of rodingitisation are estimated to have occurred under relatively moderate temperatures and pressure (~300 to 450 °C; ~2–6 kbar respectively).

1. Introduction

Rodingitisation is a Ca-metasomatic process that results after fluid/rock interaction and element transfer, commonly associated with serpentinisation of ultramafic rocks (e.g. Mittwede and Schandl, 1992; Li et al., 2007). Rodingites are formed when magmatic and/or metamorphic rocks interact with Ca-rich and Si-poor fluids previously affected by reactions with ultramafic rocks (Coleman, 1967; Frost, 1975; Evans, 1977; Bach and Klein, 2009). These metasomatic fluids contribute to the formation of Ca-rich, SiO_2-undersaturated rocks, composed of a wide variety of Ca—Al and Ca—Mg silicate minerals (Mittwede and Schandl, 1992; Li et al., 2007; Pomonis et al., 2008; Tsikouras et al., 2009; Perraki et al., 2010; Tsikouras et al., 2013; Koutsovitis et al., 2013, 2018; Hernández-Uribe et al., 2020). A typical rodingite mineral assemblage comprises of garnet, secondary clinopyroxene, chlorite, prehnite, epidote, clinozoisite and vesuvianite (Li et al., 2004, 2007; Tang et al., 2018; Wang et al., 2019). The precise determination of the mineral assemblage combined with the geochemical composition provides the basis to interpret the petrogenetic factors responsible for their formation, the evolution processes and the nature of the metasomatic agents that contribute to the transformation of the protoliths to rodingites (Bach and Klein, 2009; Tsikouras et al., 2009; Fukuyama et al., 2014; Shen et al., 2016; Koutsovitis et al., 2018; Tang et al., 2018). Several factors can influence the degree of rodingitisation such as the nature of the surrounding ultamafic rocks, the extent of serpentinisation and alteration, *P-T* (Pressure-Temperature) conditions,

* Corresponding author at: Department of Geology, Section of Earth Materials, University of Patras, GR-265 04 Patras, Greece.
E-mail address: krogkala@upatras.gr (A. Rogkala).

https://doi.org/10.1016/j.chemer.2021.125860
Received 23 June 2021; Received in revised form 13 December 2021; Accepted 18 December 2021
Available online 15 January 2022

fluid availability, water/rock ratio, CO_2 amounts and the geotectonic setting.

Potential rodingite protoliths include gabbros, diabases, pyroxenites, peridotites and less often intermediate to felsic rocks. Rodingitisation is more prominent when the protoliths are enclosed within serpentinised ultramafic rocks or are in contact with them (Schandl et al., 1989; Tsikouras et al., 2009; Li et al., 2017; Wang et al., 2019; Mubarak et al., 2020; Salvioli-Mariani et al., 2020; Duan et al., 2021a; Karkalis et al., in press). This metasomatic process preferably occurs under relatively restricted pressure/temperature conditions, affected by circulating

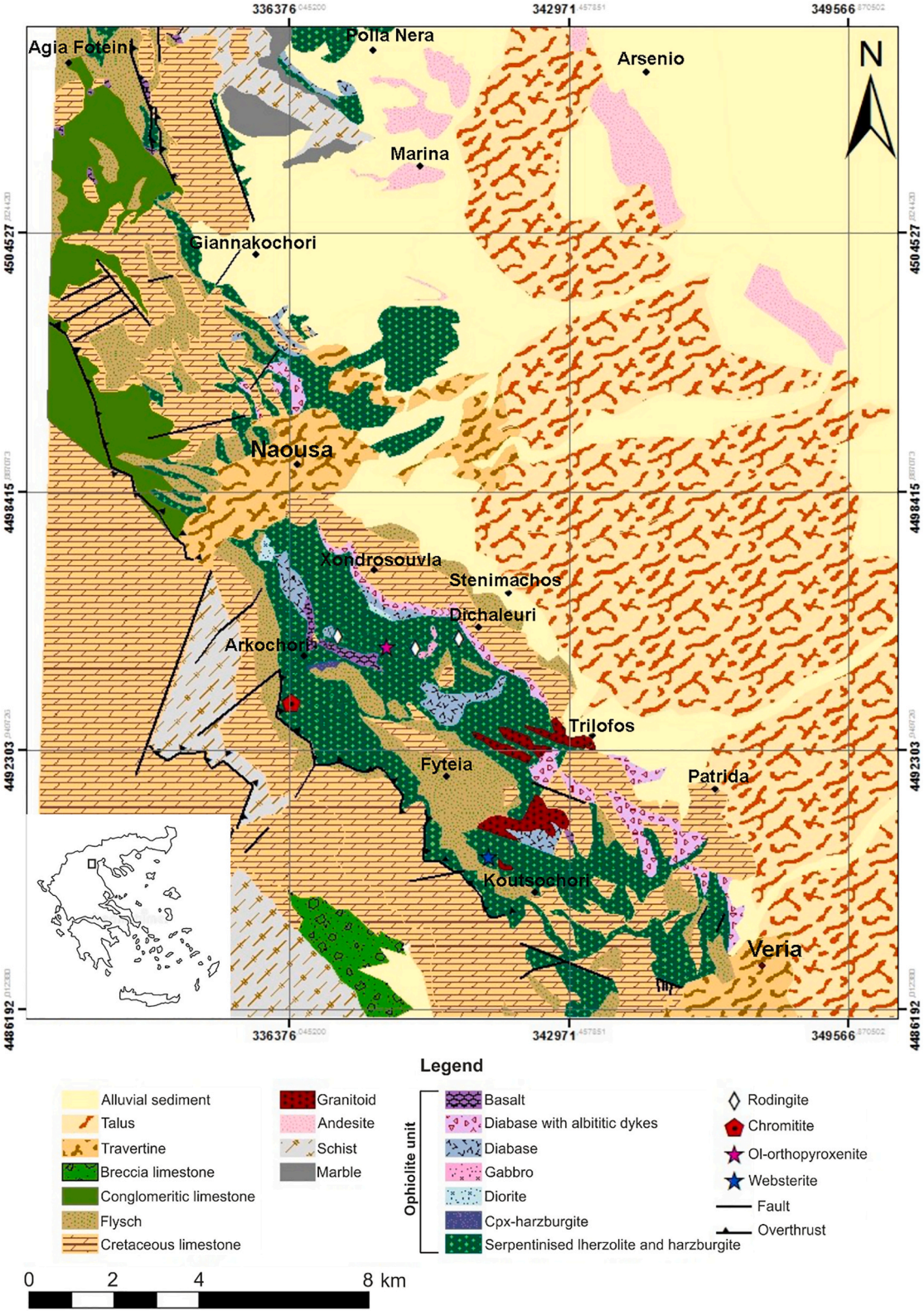

Fig. 1. Geological maps of the Veria-Naousa region (coordinates are in UTM). Inset shows the geotectonic zones of Greece highlighting the Almopias. Paikon. Peonias (from west to east) subzones of the Axios zone; black rectangle shows the study area.

hydrothermal fluids (Schandl et al., 1989; Frost et al., 2008; Li et al., 2017). Rodingites may also form at the expence of eclogite protoliths, which form under relatively high pressure/temperature conditions, derived from deep-rooted exhumation zones (Shen et al., 2016; Li et al., 2010; Duan et al., 2021b). Apart from hydrothermal circulation, rodingitisation is supported by diffusional metasomatism driven by the breakdown of Ca-silicate primary and secondary phases (e.g. diopside, plagioclase and pumpellyite) in the mafic protoliths under silica-undersaturated conditions (Bach and Klein, 2009; Frost and Beard, 2007; Frost et al., 2008).

Different types of rodingites crop out within the various ophiolitic formations in Greece and differences amongst them have been ascribed to the nature of the protoliths or to the extent of rodingitization. They preferably occur within serpentinites, either as crosscutting dykes and less often as boudins or massive outcrops (e.g. Baltatzis, 1984; Capedri et al., 1978; Serelis, 1995; Hatzipanagiotou and Tsikouras, 2001; Hatzipanagiotou et al., 2003; Pomonis et al., 2008; Tsikouras et al., 2009; Koutsovitis et al., 2013, 2018). Another factor which seems to play an important role in the type of rodingitization processes concerns the geotectonic environment; whether these occurred at fore-arc or back-arc settings. For example, rodingites in west Othris (Tsikouras et al., 2009), Kallidromon (Tsikouras et al., 2013) and Koziakas (Pomonis et al., 2008) were formed within ophiolitic formations that display back-arc affinities, whereas rodingites from east Othris (Koutsovitis et al., 2013), Evia island (Karkalis et al., 2019) and Vavdos (Sideridis et al., 2021) are related with fore-arc ophiolites.

This paper reports for the first time the occurrence of rodingites hosted within the Veria-Naousa ophiolite, aiming to i) examine the extent of rodingitisation, ii) relate the rodingites with the degrees of serpentinisation of the surrounding ultramafics, iii) define their mineralogical assemblage, iv) identify their petrogenesis in relation to their protoliths v) unravel the relation between the geotectonic setting of formation and the metasomatic processes, in relative to the *P-T* conditions and the fluid phase composition. For this purpose this study provides new petrographic, mineral chemistry, XRPD (X-ray powder diffraction) and geochemical (major and trace elements) results, focusing on determining an adequate physicochemical framework and model for the development of rodingites in the Veria-Naousa ophiolite. The outcomes from this study not only serve to interpret the petro-geochemical processes responsible for the formation of the rodingites, but also provide new insights with significant evidence for unravelling geotectonic model of formation, within the Late Jurassic to Early Cretaceous Tethyan realm.

2. Geological setting and field observations

The Veria-Naousa ophiolitic complex extends between the cities of Veria and Naousa in northern Greece (Fig. 1). This ophiolite is part of the Almopias subzone, which in turn has been derived from the Axios geotectonic zone. The Veria-Naousa ophiolite comprises of several tectonic units, which are deemed to be the southwards continuation of the Edessa ophiolite (Rogkala et al., 2019). Ophiolite emplacement occured during the Late Jurassic to Early Cretaceous in the form of imbricated thrust sheets emplaced onto the Pelagonian microcontinent, which mainly comprises of Late Triassic-Jurassic carbonate rocks (Mercier et al., 1975; Economou, 1983; Michailidis, 1990; Economou-Eliopoulos, 2003; Tsoupas and Economou-Eliopoulos, 2008; Saccani et al., 2008). The ophiolitic suite is dismembered and comprises from base to top: i) serpentinised lherzolites/harzburgites intruded by a sparse network of rodingitic, pyroxenitic, diabasic and rarely gabbroic dykes, ii) altered sheeted diabases, iii) pillow basalts. The serpentinised ultramafics are intensely tectonised and sheared, displaying a dense network of joints and deformation patterns. Pyroxenite dykes are either websterites or olivine-orthopyroxenites of variable thickness (1–5 m) (Rogkala et al., 2017). Sparse gabbroic dykes appear as intrusions within the serpentinised peridotites, most of which have been intensely rodingidised. They are medium to coarse-grained, displaying pale green colours and are exposed with a thickness ranging between 1 and 2 m. Diabase also appears in the form of dykes, whereas locally massive diabase was identified in tectonic contact with the serpentinised harzburgites and basalts. It displays dark green colours having also been locally affected by intensive rodingitisation. A cataclastic zone that includes diabasic boninitic fragments, has been cemented with albitite veins, occuring along the eastern contact of the ophiolite with the Pelagonian carbonate rocks (Fig. 1). Pillow basalts are altered and were overthrusted above the serpentinised harzburgites. Neogene to Quaternary sedimentary formations (conglomeratic limestone, breccia limestone, flysch) uncomformably overlay the ophiolite. Extensive fieldwork revealed the existence of a granitoid intrusive body, of unknown age, which penetrates the serpentinised peridotites near the village of Trilofos (Fig. 1).

The studied rodingites appear as dykes or irregular lenses within the variably serpentinised peridotites, displaying lighter colours compared to the dark-coloured ultramafic host rocks. Locally, thin pale greenish-coloured chloritic blackwall zones (up to a few cm) are found at the contact rims of rodingites and serpentinites. The relatively small outcrops of rodingites render their mapping difficult; hence their occurrences are indicated as symbols on the geological map (Fig. 1). Based upon their macroscopic features, we have distinguished the rodingites into three types: Type I rodingite appears with white to light pink colours, occurring as large lenticular blocks within serpentinised harzburgites or as dykes with local chloritic blackwall zones (Fig. 2a). It is located near to the cataclastic zone that includes diabasic fragments close the village Dichaleuri. Amongst the other rodingite types, it is characterised by its relatively high thickness (1.5–2.0 m). It is also characterised by the occurrence of chlorite-rich zones even within the inner parts of the dyke. Type II rodingite forms relatively thin (70–80 cm) coarse to medium-grained dykes cross-cutting serpentinised harzburgites (Fig. 2b). It has been recognised in the central of Veria-Naousa ophiolite close to an intrusive gabbroic body. This rodingite type tends to display whitish-colours, with a rather homogenous appearance, showing massive textures with clots of diopside, grossular and vesuvianite. It is characterised by its rather high fracture that resulted in the formation of joints. Compared to the other rodingite types, it has been less affected by seconadary chloritization processes. Type III rodingite outcrops exclusively near the Arkochori village, appearing either as fine-grained dykes or thin veins within the serpentinised harzburgites, in proximity with the diabasic dykes (Fig. 2c). They frequently display greenish colours due to the increasing participation of chlorite, at the expense of grossular-rich rodingite zones that can be distinguished due to their whitish colours (Fig. 2c).

3. Sampling and analytical methods

Twenty five rodingite and eight potential protoliths samples were collected and examined petrographically with a Leitz Ortholux II POL-BK Ltd. polarised microscope at the Department of Geology, University of Patras. The mineralogical composition of five representative rodingites, a boninitic and a tholeiitic diabase and a gabbro was further identified with powder X-ray diffraction (XRPD) analysis, using a Bruker D8 Advance Diffractometer (Bruker, Billerica, MA, USA), with Ni-filtered CuKα radiation. The scanning area for bulk mineralogy of the samples covered the 2θ interval 2–70°, with a scanning angle step size of 0.015° and a time step of 0.1 s. The mineral phases were determined using the DIFFRACplus EVA 12® software (Bruker-AXS, Billerica, MA, USA) based on the ICDD Powder Diffraction File of PDF-22006. The semi-quantitative analyses were performed by TOPAS 3.0 ® software (TOPAS MC Inc., Oakland, CA, USA), based on the Rietveld method refinement routine. The routine is based on the calculation of a single mineral-phase pattern according to the crystalline structure of the respective mineral, and the refinement of the pattern using a non-linear least squares routine. The quantification errors were calculated to Bish and Post (1993), and they are estimated to be ~1%. TOPAS results

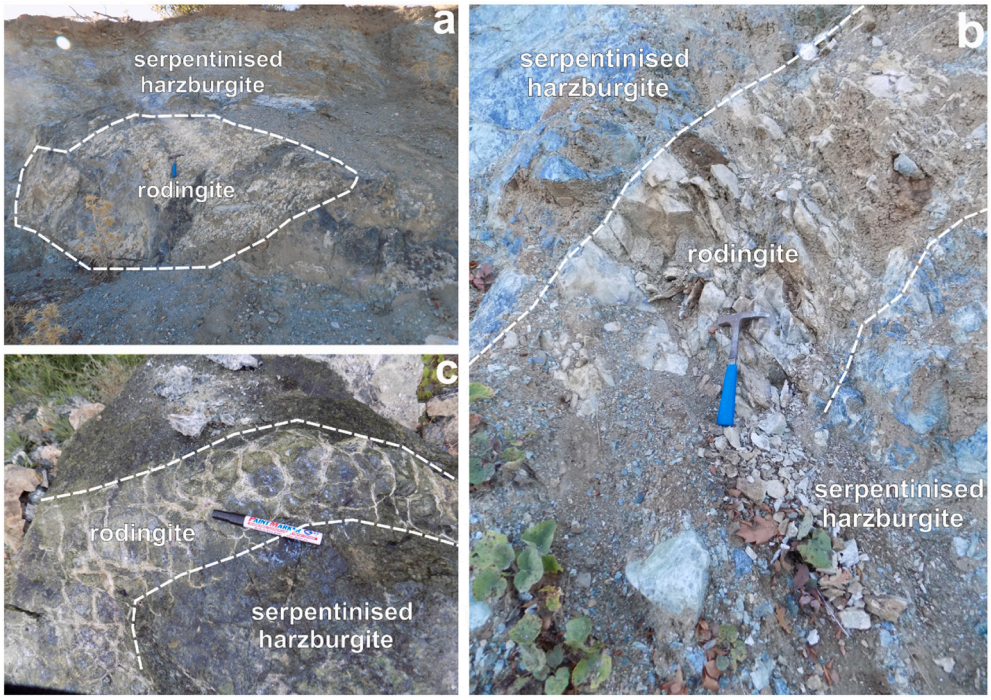

Fig. 2. (a) Subhorizontal whitish rodingite lense in sharp contact with serpentinised harzburgite from the region of Dihaleuri. (b), (c) Rodinditised dykes within serpentinised harzburgite from Arcohori with variable width.

coupled with point counting were used to estimate the modal mineralogical composition of the studied rocks (Supplementary Table 1).

Mineral chemistry analyses were performed using a JEOL JSM-6300 SEM equipped with energy dispersive and wavelength dispersive spectrometers and INCA software at the Laboratory of Electron Microscopy and Microanalysis, University of Patras. Operating conditions were accelerating voltage 25 kV and beam current 3.3 nA, with a 4 μm beam diameter. The total counting time was 60 s and dead-time 40%. Synthetic oxides and natural minerals were utilised as standards for our analyses. Detection limits are ~0.1% and accuracy better than 5% was obtained. Whole-rock chemical analyses for major and trace elements were performed at Bureau Veritas Mineral Laboratories at Vancouver (Canada). Major element analyses were carried out using a Spectro Ciros Vision ICP-ES for major elements as well as Cr, Ni and a Perkin–Elmer–Elan 6000/9000 ICP-MS for all other trace elements and REE. Loss on ignition (LOI) was determined using the weight loss after 90 min of heating at 950 °C, whereas total carbon was analysed by Leco. Detection limits for major and trace elements range from 0.01 wt% to 0.04 wt% and from 0.01 ppm to 10 ppm, respectively. The analytical precision calculated from replicate analyses is better than 3% for most major elements and better than 5% for trace elements.

4. Results

4.1. Veria-Naousa rodingite types – a brief overview

The three rodingite types display different textural characteristics, mineral assemblages and geochemical affinities. In brief, Type I rodingites are characterised by the presence of garnet, clinopyroxene, chlorite and the absence of vesuvianite, displaying high contents of Cr and Ni. Type II rodingites encompass relatively high amounts of garnet compared to the other two types, resulting in enhanced Ca contents. Type III rodingites are fine-grained and are characterised by the rather frequent presence of vesuvianite, andradite and chlorite, exhibiting relatively high Fe contents compared to the other two types. The following subchapters describe in detail the petrographic, mineral chemistry and geochemical results obtained from the three types of rodingites and their associated protoliths.

4.2. Petrographic properties and features

4.2.1. Protolith mineral assemblages

The mafic section of the Veria-Naousa ophiolite comprises of diabases and gabbros that were subjected to low-grade oceanic alteration processes prior to rodingitisation. Diabase exhibits boninitic affinities (see § 4.4), displaying porphyroid and subophitic textures (Fig. 3a, b). Its primary assemblage includes plagioclase, clinopyroxene, magnesiochromite, magnetite and accessory apatite. Secondary minerals include epidote, chlorite, fibrous amphibole (mostly actinolite), hematite and titanite (Fig. 4a, Supplementary Table 1). Plagioclase phenocrysts are euhedral, medium grained (400–500 μm) with a modal composition of 35–40 vol% (Supplementary Table 1). Clinopyroxene grains are most often subhedral, medium grained (300–400 μm), appearing less frequently (~10 vol%). Actinolite formed at the expense of clinopyroxene and magmatic hornblende attributed to uralitisation phenomena. Few rare amygdales infilled with chlorite and albite are observed in some parts of the boninitic diabase.

Gabbro is medium to coarse grained, although in cases textures are pegmatitic (Fig. 3c). Primary textural features have been preserved, displaying subophitic and rarely ophitic textures. Its primary assemblage consists mainly of plagioclase, clinopyroxene and hornblende (Fig. 4c, Supplementary Table 1). Ilmenite, magnetite, titanite and apatite are accessory mineral phases, wheras secondary minerals comprise of actinolite, epidote, prehnite and chlorite. Actinolite was formed at the expense of primary mineral phases such as clinopyroxene and magnesiohornblende.

Diabase of tholeiitic affinity (see § 4.4) exhibits porphyroid and subophitic textures (Fig. 3d). Coarser crystals are relatively rare comprising of subheral clinopyroxene, plagioclase and scarce hornblende (Fig. 4b, Supplementary Table 1) surrounded by fine grained plagioclase and clinopyroxene laths or anhedral small-sized grains. Accessory minerals include quartz, magnetite, ilmenite, apatite and titanite. In many samples, plagioclase phenocrysts are partly altered to sericite, whereas clinopyroxene grains have been variably altered to

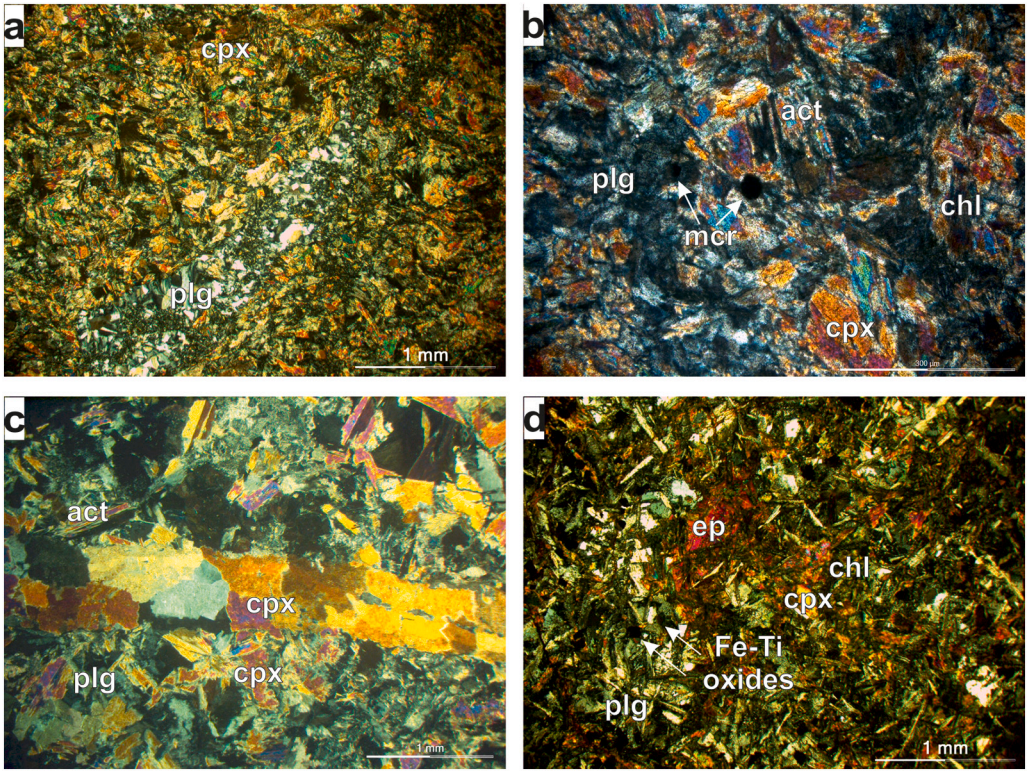

Fig. 3. Photomicrographs of textural characteristics of rodingite protoliths from the Veria-Naousa mafic rocks showing: a. Fine to medium-grained boninitic diabase with plagioclase (plg) and clinopyroxene (cpx) (sample BE.79, Nicols +); b. Subophitic texture along with plagioclase (plg), altered clinopyroxene (cpx) to chlorite (chl) and actinolite (act), as well as few magnesiochromite (mcr) crystals in a boninitic diabase (sample BE.43, Nicols +); c. Ophitic texture, both plagioclase (plg) and clinopyroxene (cpx) display irregular shapes, in gabbro. Secondary actinolite (Act) at the rims of clinopyroxene (cpx) (sample BE.29; Nicols +); d. Subophitic texture along with plagioclase (plg), altered clinopyroxene (cpx) to epidote (ep) and chlorite (chl), as well as relatively abundant Fe—Ti oxides in diabase sample (BE.48, Nicols +).

chlorite, epidote, prehnite and actinolite. Quartz and epidote-rich late-stage thin veins occasionally cross-cut the samples.

4.2.2. *Type I rodingites*

Rodingites of this type display the mineralogical assemblage of garnet + clinopyroxene + chlorite. Accessory phases include relict magnetite and sulphide phases (pyrite and galena) (Fig. 4d, Supplementary Table 1). They exhibit granoblastic, lepidoblastic, porphyroblastic and cataclastic textures (Fig. 5a). Garnet occurs either as relatively coarse and idiomorphic grained forming cataclastic textures or as fine to medium grained subidiomorphic crystals forming granoblastic segregations dispersed within the rodingite. Petrographic observations suggest that they have been formed after primary clinopyroxene. The vast majority of clinopyroxene grains are neoblasts, which are often associated with garnet. Relic primary clinopyroxene is rare and is altered to chlorite and minor tremolite (Fig. 5b). Chlorite developed fine-grained segregations throughout the rocks. Relict magnesiochromite has been preserved, although their rims were affected by metasomatism (Fig. 5b).

4.2.3. *Type II rodingites*

The Type II rodingites are characterised by the mineralogical assemblage clinopyroxene + garnet + vesuvianite ± quartz. Accessory phases include Fe—Ti oxides, apatite and baryte (Fig. 4e, Supplementary Table 1). These rocks display blastophitic to blastosubophitic texture and locally nematoblastic and lepidoblastic textures (Fig. 5c). Clinopyroxene appears as relict magmatic crystals inherited from the gabbroic protoliths, as well as neoblastic grains, which were formed during rodingitisation. Frequently, relict clinopyroxene is altered to chlorite at the rims. Clinopyroxene neoblasts commonly appear as subhedral grains alongside with garnet and vesuvianite (Fig. 5c). Garnet mostly occurs as fine-grained segregations within the rodingite and locally forms monomineralic assemblages. In some cases, garnet has pseudomorphically replaced magmatic plagioclase (Fig. 5d). Vesuvianite comprises of weakly birefringent, fine to medium-grained crystals with anomalous deep-purple polarizing colours. It appears either as granoblastic segregations dispersed within the rodingite along with clinopyroxene and/or small garnet grains (Fig. 5e). Accessory fine grained baryte occurs throughout the samples groundmass and in some cases is enclosed within garnet grains. Sporadic apatite is present either as individual crystals or more commonly within garnet and clinopyroxene grains.

4.2.4. *Type III rodingites*

Type III rodingites include the mineralogical assemblage grossularitic garnet + andraditic garnet + vesuvianite + clinopyroxene + chlorite. Accessory phases comprise of Fe—Ti oxides (magnetite, ilmenite) (Fig. 4f, Supplementary Table 1). They mostly display granoblastic, nematoblastic and blastosubophitic textures (Fig. 5f, g). Locally, relic subophitic textures have been preserved suggesting that these rocks were derived from diabasic protoliths. Another inherited magmatic mineral phase is represented by the occurrence of plagioclase relics, which have been partially replaced by sericite. Grossularitic garnet usually occurs as fine-grained segregations along with vesuvianite and neoblastic clinopyroxene. Andradite garnet is a late-stage phase, as indicated by the fact that it is found surrounding the grossular grains at their rims (Fig. 5f). Vesuvianite comprises of coarse to medium-grained crystals with anomalous brownish-yellow polarizing colours. It appears either as granoblastic segregations along with small-sized neoblastic clinopyroxene, chlorite and/or garnet grains (Fig. 5h). Neoblastic clinopyroxene is either subhedral or anhedral most often as fine grained crystals. Relict clinopyroxene grains have been locally replaced by garnet and chlorite. Chlorite appears intragranularly between neoblastic clinopyroxene and vesuvianite, or occasionally overgrowing primary clinopyroxene.

4.3. *Mineral chemistry*

4.3.1. *Mineral chemistry of protoliths*

In the boninitic diabases, plagioclase is classified as albite (Supplementary Table 7), likely attributed to secondary low-grade albitisation processes. Amphibole is represented by actinolite (nomenclature of

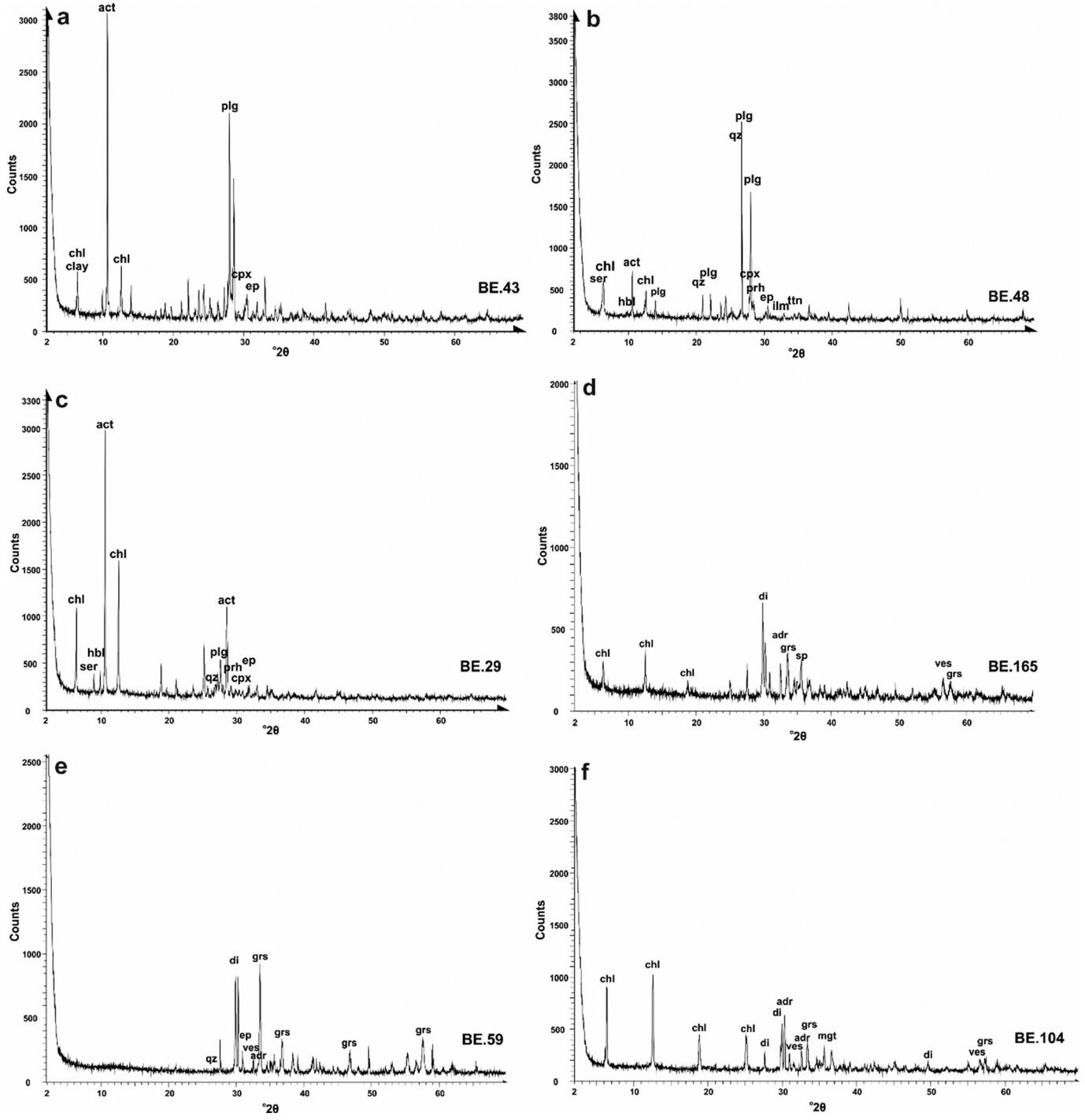

Fig. 4. X-ray diffraction patterns of the representative studied samples: (a) Boninitic diabase (sample BE.43); (b) tholeiitic diabase (sample BE.48); (c) gabbro (sample BE.29); (d) Type I rodingites (sample BE.165); (e) Type II rodingites (sample BE.59); (f) Type III rodingites (sample BE.104); (Abbreviations: act: actinolite, adr: adrandite, chl: chlorite, clay: clay minerals, cpx: clinopyroxene, di: diopside, ep: epidote, hbl: hornblende, grs: grossular, ilm: ilmenite, mgt: magnetite, plg: plagioclase, prh: prehnite, qz: quartz, ser: sericite, sp.: spinel, ttn: titanite, ves: vesuvianite).

Leake et al., 1997; Supplementary Table 8) displaying slightly variable Si, Ti, Al^{vi} and Fe^{t} values per formula unit (p.f.u) (7.556–7.826, 0.010–0.042, 0.166–0.403, 1.041–1.396, respectively). Following the nomenclature of Morimoto (1988), clinopyroxene in the boninitic diabase is classified as augite (Supplementary Table 2), exhibiting Mg# [=100 × Mg/(Mg + Fe^{2+})] values from 81.3 to 89.7; X_{Na} [= Na/(Na + Ca)] varying from 0.01–0.13. Using charge balance, calculated Al^{vi} and Fe^{t} are relatively high (0.111–0.179 and 0.104–0.211 p.f.u., respectively). Magnesiochromite grains have been identified in boninitic diabase. Representative microanalyses of magnesiochromite are given in Supplementary Table 6. They display relative Cr# [=100 × Cr/(Cr + Al)] (76.9–84.8) and Mg# values (47.7–50.4). Chlorite is classified as pycnochlorite (following the nomenclature of Hey, 1954) with moderate Al^{vi} (2.519–2.586 p.f.u.) values and $Fe^{t}/(Fe^{t} + Mg)$ ratios (0.28–0.30) (Supplementary Table 5). Epidote grains are compositionally homogenous with highly comparable Fe^{3+} and Al contents (Supplementary Table 9), displaying moderate pistacitic values (Ps = $100*Fe^{3+}/(Fe^{e3+}+Al)$ ranging from 16.50 to 20.27. Most prehnite grains

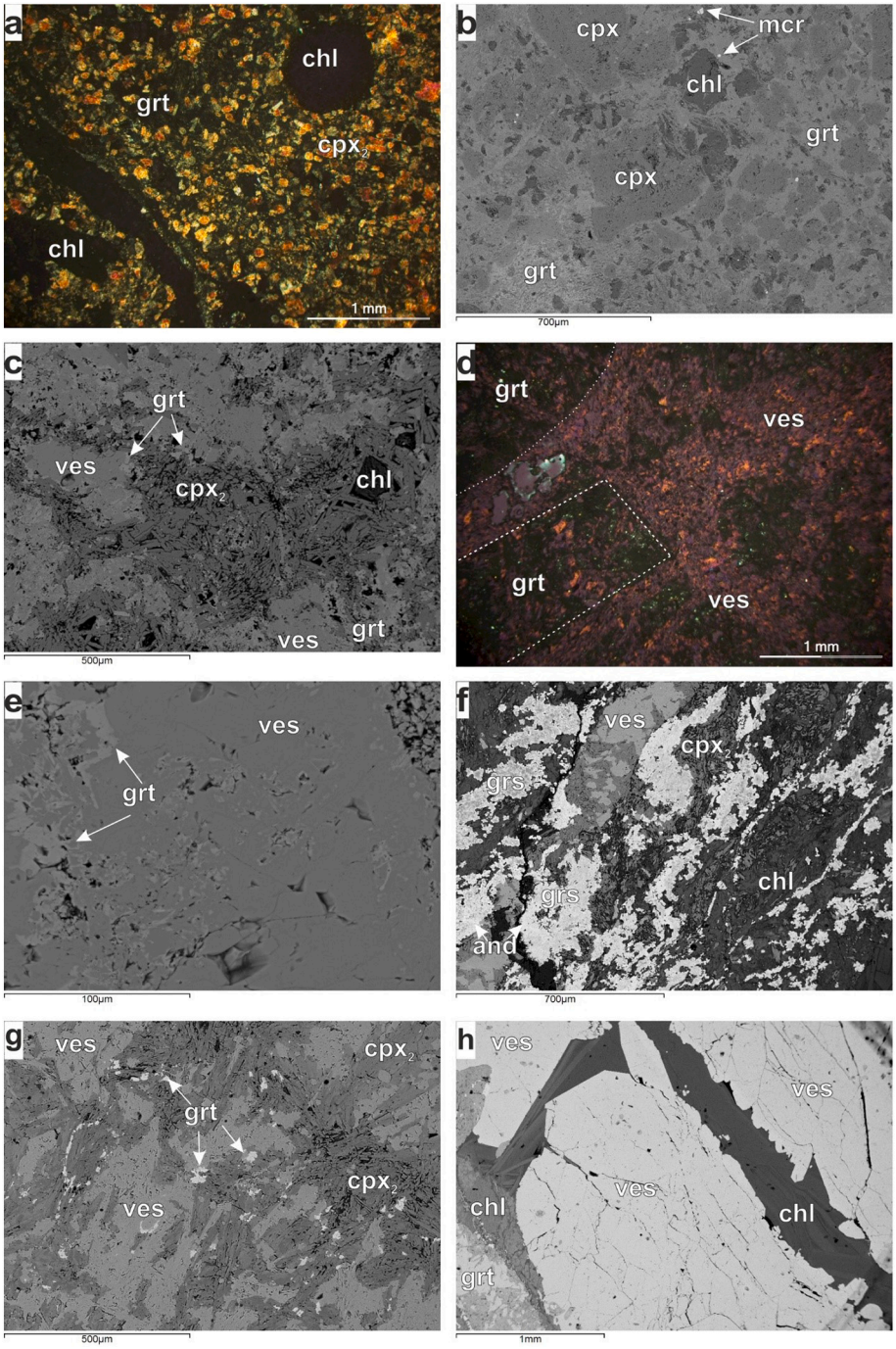

Fig. 5. Textural and metasomatic characteristics of Type I-III rodingites from the Veria-Naousa ophiolite: (a) Photomicrograph of neoblastic clinopyroxene (cpx_2) associated with garnet (grt) and chlorite (chl) (Type I, sample BE.165, Nicols +), (b) Backscattered electron image of relics of clinopyroxene (cpx), chlorite (chl), garnet (grt) and magnesiochromite (mcr) in rodingite derived from boninitic diabase (Type I, sample BE.165), (c) Backscattered electron image of neoblastic clinopyroxene (cpx_2), which formed chlorite (chl) and surrounded by garnet (grt) and vesuvianite (ves) (Type II, sample BE.59), (d) Photomicrograph of garnet (grt) with blastophitic texture in association with vesuvianite (ves) and has replaced magmatic plagioclase (white outline) (Type II, sample BE.64, Nicols +), (e) Backscattered electron image of vesuvianite (ves) replacing garnet (grt) (Type II, sample BE.25), (f) Backscattered electron image of subophitic texture in rodingite with two generations of garnet [grossularitic garnet (grs) and andraditic garnet (and)], vesuvianite (ves) and neoblastic clinopyroxene (cpx_2) which has been replaced by chlorite (chl) (Type III, sample BE.110), (g) Backscattered electron image of vesuvianite (ves) and garnet (grt) along with scattered neoblastic clinopyroxene (cpx_2) (Type III, BE.104), (h) Backscattered electron image of granoblastic segregations of vesuvianite (ves) surrounding with chlorite (chl) and garnet (grt) (Type III, sample BE.104).

(Supplementary Table 10) exhibit relatively low Fe^t and Mg values (0.009–0.036 and 0.023–0.065 p.f.u., respectively).

Amongst the primary mineral constituents of tholeiitic diabase and gabbro, plagioclase crystals (Supplementary Table 7) are secondary albites ($Ab_{95.6–99.2}An_{0.4–1.4}Or_{0.2–3.1}$) and labradorite ($Ab_{30.2–39.6}An_{60.4–69.8}Or_{0.0–0.3}$), whereas andesine ($Ab_{53.1}An_{46.3}Or_{0.6}$) occurs less frequently. Relict amphiboles are classified as magmatic magnesiohornblende, as well as secondary actinolite and ferroactinolite (nomenclature of Leake et al., 1997; Supplementary Table 8). Magnesiohornblende grains display a compositon with rather consistant Si, Ti, Al^{vi} and Na (7.225–7.458, 0.057–0.140, 0.100–0.218, and 0.102–0.254 p.f.u., respectively). Based on detailed petrographical observations (e.g. subhedral brown-coloured grains) and evaluation of the mineral chemistry data (restricted Si, enhanced Al, Ti and Na) magnesiohornblende was likely of magmatic rather than metamorphic origin. Secondary amphiboles are represented by fibrous textured actinolite and ferroactinolite, with enhanced Si and Fe^{2+} contents (7.519–7.900 and 1.804–3.285 p.f.u, respectively), compared to the magnesiohornblende. Clinopyroxene grains are diopside or augite (Supplementary Table 2), displaying variable Mg# (68.5–90.6) and moderate Wo component (37.2–44.7). Their Al, Fe^t, and Cr values are comparable with those identified in the boninites. Chlorite appears in both boninitic diabases and gabbros, with similar $Fe^t/(Fe^t + Mg)$ ratios (0.40–0.48) (Supplementary Table 5). According to the nomenclature of Hey (1954), chlorite is classified as pycnochlorite and diabantite, whereas ripidolite occurs less frequently. Epidote grains are compositionally inhomogeneous with variable Fe^{3+} and Al contents, which also reflect a wide range in the pistacitic content (18.47–29.52;

Supplementary Table 9). Prehnite (Supplementary Table 10) exhibit relatively higher Fe^t values (0.014–0.064 p.f.u.) compared to prehnite in boninites, with the highest values corresponding to prehnite that formed at the expense of magnesiohornblende. The enhanced Fe contents in both epidote and prehnite suggest relatively high oxygen fugacity conditions compared to those estimated in the boninites.

4.3.2. Mineral chemistry of rodingites

4.3.2.1. Clinopyroxene. Representative clinopyroxene microanalyses from the Veria-Naousa rodingites are displayed in Supplementary Table 2. Both the inherited relict clinopyroxenes and the secondary clinopyroxene neoblasts are classified as diopsides (following the IMA nomenclature of Morimoto, 1988). Primary clinopyroxene has been identified in Type I and III rodingites. Within Type I rodingites, relict clinopyroxene grains exhibit higher Al (0.023–0.114 p.f.u.) and Fe^t (0.138–0.220 p.f.u.) values, as well as slightly lower Mg# values (84.4–93.2), compared to relict clinopyroxenes of Type III rodingites ($Al^{vi} < 0.040$, $Fe^t = 0.039–0.075$ p.f.u., Mg# = 91.9–95.7). Neoblastic clinopyroxenes of Type II and III rodingites are relatively enriched in Ca compared to those occurring within Type I rodingites, whereas Al^{vi} values of the former are lower. Regardless of the type of rodingite, secondary clinopyroxene neoblasts exhibit relatively higher Ca (0.744–1.012 p.f.u.), Mn (0.006–0.027 p.f.u.) and higher Mg# values (84.8–97.7) compared to the relict ones. The neoblastic clinopyroxenes of Type I display high contents of Cr (0.026–0.041 p.f.u.) compared to those from the other two types.

4.3.2.2. Garnet. Representative garnet microanalyses from the rodingites are listed in Supplementary Table 3 and Supplementary Fig. S1. Fe^{3+}/Fe^{2+} partitioning was calculated on a stoichiometric basis; most iron in these garnets usually occurs in the trivalent state. The early-stage garnet grains are grossular-rich ($Adr_{6.73–43.98}$, $Grs_{54.63–93.27}$), which are often corroded and fractured. Late-stage garnet exhibts increased andradite component ($Adr_{42.61–82.67}$, $Grs_{14.11–38.62}$).

The analysed garnets in Type I rodingites display homogeneous chemical compositions, in which grossular is the most prominent end-member, whereas andradite is the most abundant substitute. All display low contents of Si (2.954–3.288 p.f.u.) and Fe^{3+} (0.205–0.423 p.f.u.), as well as high Ca (2.675–3.098 p.f.u.) and Al^{vi} (1.217–1.638 p.f.u.) compared to garnets from the other two Types of rodingites. Garnets in Type II and III rodingites show irregular compositional heterogeneities, mainly due to variations in Ca, Al^{vi} and Fe^{3+}. They contain grossular components with variable substitutions including a prominent andradite component; these are characterised by their higher Ti values (0.015–0.556 p.f.u.) compared those of Type I (Table S3).

4.3.2.3. Vesuvianite. Representative microanalyses of vesuvianite are listed in Supplementary Table 4. Mineral formulae were calculated on the basis of 50 cations, according to Fitzgerald et al. (1992). Vesuvianite crystals are found only in Type II and III rodingites. The analysed vesuvianite crystals of Type II rodingites are characterised by higher Mg and lower Ti contents compared to those of Type III. The analysed vesuvianite of Type III rodingites displays high Fe^{3+} and low Mn contents compared to those of Type II. Low totals for these analyses suggest the existence of a volatile components in their crystal structure.

4.3.2.4. Chlorite. Representative microanalyses of chlorite from the studied rodingites are given in Supplementary Table 5. Chlorite is a relatively frequent phase in Type I and III rodingites whereas it is an accessory phase in Type II rodingites. Chlorites of the Type I rodingites are compositionally constant regarding their Al^{vi} (1.935–2.417 p.f.u.) contents and their $Fe^t/(Fe^t + Mg)$ ratios (0.19–0.24). According to the nomenclature of Hey (1954), they are classified as penninite and diabantine. Type III rodingites include chlorite crystals that display a broader compositional range reflected from their varability in the Al^{vi} (1.982–2.578 p.f.u.) contents and in their $Fe^t/(Fe^t + Mg)$ values (0.05–0.27). Most are classified as pychnochlorite and penninite, whereas diabantite occurs as an accessory phase.

4.3.2.5. Spinel-group minerals. Few relict magnesiochromite grains have been identified in Type I rodingites, inherited from the boninitic diabase precursor. Representative microanalyses of magnesiochromite are given in Supplementary Table 6. They display relatively narrow Cr# and Mg# values (76.7–83.1 and 44.3–59.5, respectively). Al^{vi} values are low, ranging from 0.386 to 0.439 p.f.u. Rims have slightly higher Fe^t and lower Mg compared to the cores, attributed to the effects of metasomatism.

4.4. Whole-rock chemistry

Whole-rock chemical analyses from the Veria-Naousa rodingites and their protoliths are listed in Table 1. Based on the major element chemistry of the protoliths, these correspond to three disnct lithotypes: i) diabase with boninitic affinities, ii) tholeiitic gabbro, iii) diabase with tholeiitic affinities. The first lithotype contains relatively high amounts of MgO (10.56 wt%) and MgO/FeO ratio (1.64), as well as low TiO_2 contents (0.22 wt%), compared to those of gabbro (8.70 wt%, 0.94 and 0.33 wt% respectively) and the tholeiitic diabase (2.92 wt%, 0.28 and 0.70 wt% respectively). Following the Le Bas (2000) classification of high-Mg rocks, the first lithotype geochemically corresponds to a boninite ($SiO_2 > 52$ wt%, MgO > 8 wt%, $TiO_2 < 0.5$ wt%). CaO, K_2O and Al_2O_3 contents (8.70, 4.75 and 14.44 wt% respectively) are higher in the gabbro protolith compared to the other two lithotypes; the high —K amounts suggest a calc-alkaline affinity for the gabbro. Cr (493 ppm), Cu (202.8 ppm) and Pb (13.5 ppm) contents are significantly higher in the boninitic diabase. MORB-normalised REE patterns of the boninitic diabase (Fig. 7a) display slightly lower MREE contents relevant to the LREE, whereas the HREE are rather enhanced. The ΣREE contents (see Table 1) and the shape of the REE normalised pattern are consistent with those of the high-Si boninites described by Umino et al. (2015).

The MORB-normalised REE pattern of the gabbro presents relatively moderate to low ΣREE values (Table 1), exhibiting moderate LREE, similar to slightly lower MREE and similar HREE (Fig. 7b). Compared with the boninite, the tholeiitic diabase has lower MgO contents and rather higher Al_2O_3 and TiO_2 contents. The MORB-normalised REE pattern of the tholeiitic diabase (Fig. 7c) can be regarded as being relatively flat.

Rodingites are distinguished into three types in terms of petrographic and mineralogical criteria, which is also reflected in their whole-rock chemistry, most notably in the SiO_2, Al_2O_3, MgO, Fe_2O_3, CaO and LOI contents. The studied rodingites are enriched in CaO and depleted in SiO_2 compared to their protoliths. Type I rodingites generally have higher Cr, Ni, Pb contents (1006–1067 ppm, 308.7–334.1 ppm, 6.4–8.4 ppm) and lower TiO_2, Fe_2O_3, V (0.28–0.30 wt%, 7.47–7.77 wt%, 183–189 ppm) contents compared to the other types of rodingites. Type II rodingites exhibit high CaO (30.65–35.09 wt%) and Al_2O_3 (9.89–14.47 wt%), as well as low SiO_2 (37.12–41.70 wt%,), MgO (2.66–6.23 wt%) and alkali contents. Type III rodingites are enriched in SiO_2 (41.00–43.54 wt%), Fe_2O_3 (10.12–10.54 wt%), MgO (11.16–13.26 wt%), displaying relatively low CaO (18.42–20.95 wt%) compared to the other two types. Type I and III rodingites present higher LOI values (3.5–5.6) when compared to the Type II rodingites (2.5–2.8). On the SiO_2 vs. CaO binary diagram (Fig. 6a), it seems that the Type I and III rodingites show considerable similarities with the Othris rodingites, likely attributed to fact that their degree of rodingitisation was higher compared to rodingites from Iti and lower from those from the Koziakas and Abitibi. On the other hand, Type II rodingites exhibit higher CaO concentrations being more comparable with rodingites from Koziakas and Abitibi. Similar interpretations can be derived when plotting the

Table 1
Whole-rock major, trace element and REE compositions of representative rodingites samples and their protoliths from Veria-Naousa ophiolite (– below detection limit).

Rodingite Type	Type I		Boninite diabase	Type II			Gabbro	Type III		Diabase
	BE.165	BE.154	BE.43	BE.25	BE.59	BE.64	BE.29	BE.104	BE.110	BE.48
Major elements (wt%)										
SiO_2	42.82	41.35	57.17	37.12	41.70	37.5	50.02	41.00	43.54	59.48
TiO_2	0.28	0.30	0.22	0.36	0.39	0.35	0.33	0.61	0.64	0.70
Al_2O_3	9.38	9.31	11.68	14.47	9.89	14.15	14.44	7.77	8.49	13.51
$Fe_2O_3^t$	7.47	7.77	7.14	7.58	8.22	7.82	10.26	10.12	10.54	11.51
MnO	0.14	0.14	0.15	0.12	0.16	0.12	0.16	0.18	0.17	0.13
MgO	11.62	12.26	10.56	2.66	6.23	2.57	8.70	13.26	11.16	2.92
CaO	24.31	23.92	5.88	35.09	30.65	34.76	7.06	20.95	18.42	3.78
Na_2O	0.02	0.07	4.89	0.01	0.02	0.02	0.67	0.03	1.47	4.82
K_2O	0.01	0.01	0.26	0.01	0.01	0.01	4.75	0.02	0.01	0.25
P_2O_5	0.02	0.02	0.02	0.01	0.02	0.01	0.01	0.04	0.04	0.03
LOI	3.5	4.4	1.7	2.5	2.5	2.8	3.7	5.6	5.1	2.7
TOT/C	0.02	0.08	0.01	0.02	0.04	0.03	0.02	0.02	0.02	0.02
Total	99.56	99.54	99.65	99.90	99.76	99.93	99.29	99.56	99.57	99.83
Trace elements (ppm)										
Cr	1006	1067	493	14	192	230	349	397	276	14
Co	43.7	45.3	32.5	29.0	26.3	27.2	45.0	58.1	46.26	15.3
Ni	308.7	334.1	51.2	13.0	22.5	30.3	170.5	168	135.7	26.6
Cu	10.7	25.0	202.8	76.7	152.1	67.4	3.1	10.7	47.6	153.9
Zn	32	34	25	18	10	27	19	21	25.6	43
Rb	0.4	1.2	2.6	0.5	0.5	0.2	60.0	0.3	0.6	3.0
Sr	26.6	32.9	49.0	5.4	2.5	4.3	1156.4	68.3	71.4	79.1
Y	9.5	9.9	13.3	11.6	12.3	11	8.9	15.4	16.1	17.1
Zr	18.9	17.3	11.4	11.7	12.2	11.8	11.2	21.2	23.9	27.7
Nb	0.4	0.6	0.8	0.3	0.4	–	0.4	0.2	0.5	1.1
Pb	6.4	8.4	13.5	2.8	6.8	0.4	9.5	1.3	2.6	4.0
Ba	6	11	21	2	2	5	2966	3	13	31
V	189	183	177	242	259	241	237	391	388	373
Sc	31	32	32	27	33	26	41	54	49	38
Ga	6.5	7.5	8.1	9.7	7.2	6	13.6	0.9	2.6	13.4
Hf	0.5	0.5	0.5	0.6	0.5	0.5	0.4	0.9	0.9	1.1
As	2.1	2.4	–	0.6	–	–	–	–	–	0.7
Hg	–	–	–	–	–	–	–	–	–	–
Ta	–	–	–	–	–	–	–	–	–	–
Th	–	–	–	–	0.2	–	0.2	0.3	0.4	0.7
U	–	–	–	0.2	0.2	0.2	0.1	0.1	0.1	0.3
Be	–	–	–	–	–	–	1	–	–	–
Au (ppb)	3.3	2.9	1.9	1.2	4.1	–	0.6	–	–	3.9
REE (ppm)										
La	1.6	1.8	1.4	1.5	1.6	0.7	1.5	1.3	1.5	2.1
Ce	3.1	3.6	2.3	2.0	2.5	1.7	2.4	4	4.1	3.8
Pr	0.45	0.52	0.36	0.30	0.35	0.24	0.34	0.56	0.53	0.59
Nd	2.5	2.7	2.1	1.8	2.0	1.4	1.7	3.2	3.3	3.2
Sm	0.77	0.83	0.98	0.84	0.80	0.62	0.69	1.05	1.08	1.19
Eu	0.25	0.24	0.23	0.48	0.34	0.38	0.26	0.37	0.41	0.44
Gd	1.08	0.94	1.39	1.39	1.42	1.23	1.12	1.87	1.9	1.94
Tb	0.22	0.19	0.29	0.25	0.27	0.23	0.20	0.33	0.35	0.42
Dy	1.60	1.46	2.15	1.90	1.90	1.72	1.44	2.51	2.63	3.06
Ho	0.35	0.31	0.53	0.44	0.44	0.37	0.30	0.55	0.57	0.66
Er	1.09	0.93	1.50	1.24	1.41	1.25	1.03	1.77	1.93	2.19
Tm	0.17	0.19	0.25	0.21	0.22	0.19	0.17	0.26	0.29	0.33
Yb	1.12	0.98	1.51	1.51	1.48	1.32	1.00	1.82	1.93	2.22
Lu	0.16	0.13	0.26	0.23	0.26	0.21	0.21	0.3	0.32	0.35
MgO/FeO^t	1.73	1.75	1.64	0.39	0.84	0.37	0.94	1.45	1.18	0.28
Al_2O_3/CaO	0.39	0.39	1.99	0.41	0.32	0.41	2.05	0.37	0.46	3.57

studied rodingites on the $Na_2O + K_2O$ vs. CaO binary diagram (Fig. 6b). Rodingites and their protoliths have also been plotted on the ACF ternary diagram (Fig. 6c). The Type I and III rodingites are projected within the Othris compositional field, whereas Type II rodingites plot close or within the Coleman field. The latter differ from the Type I and III rodingites due to their higher abundance in grossular and vesuvianite (Fig. 6c).

The REE contents of the rodingite samples can be categorised in three different geochemical groups (Fig. 7), as shown in the MORB-normalised REE patterns (Fig. 7a-c). Type I rodingites display relatively flat REE patterns with a weak LREE enrichments, along with slight negative Eu anomalies. Their MREE and HREE concentrations are gently lower relative to the protolith (Fig. 7a). Type II rodingites show slightly positive slopes from the LREE to the HREE (except for La) with weak Eu positive anomalies, likely inherited from their gabbroic protoliths (Fig. 7b). In Type III rodingites, the differences between the normalised REE are insignificant, with some of the LREE being slightly depleted (Fig. 7c).

4.5. Isocon analysis and element transfer

The isocon method (Grant, 1986, 2005) is a graphical approach aimed to determine major and trace elements modifications between metasomatic rocks and their protoliths. According to this method, the

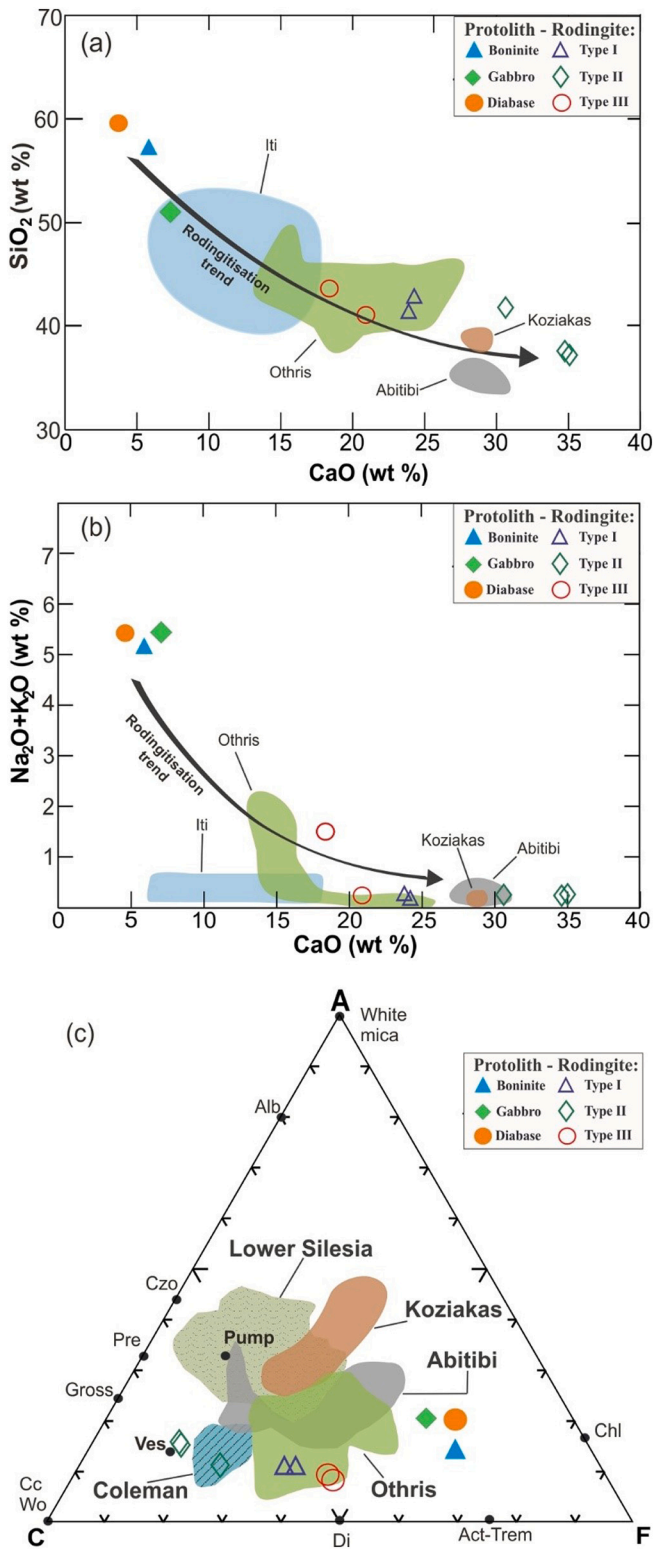

Fig. 6. (a); (b) Binary diagrams of SiO_2 (wt%) vs. CaO (wt%) and $Na_2O + K_2O$ (wt%) vs. CaO (wt%); (c) ACF diagram for rodingites and their protoliths showing their compositional variations. Fields data from: Coleman, 1977, Schandl et al., 1989, Dubińska, 1997, Pomonis et al., 2008, Koutsovitis et al., 2013, Tsikouras et al., 2013.

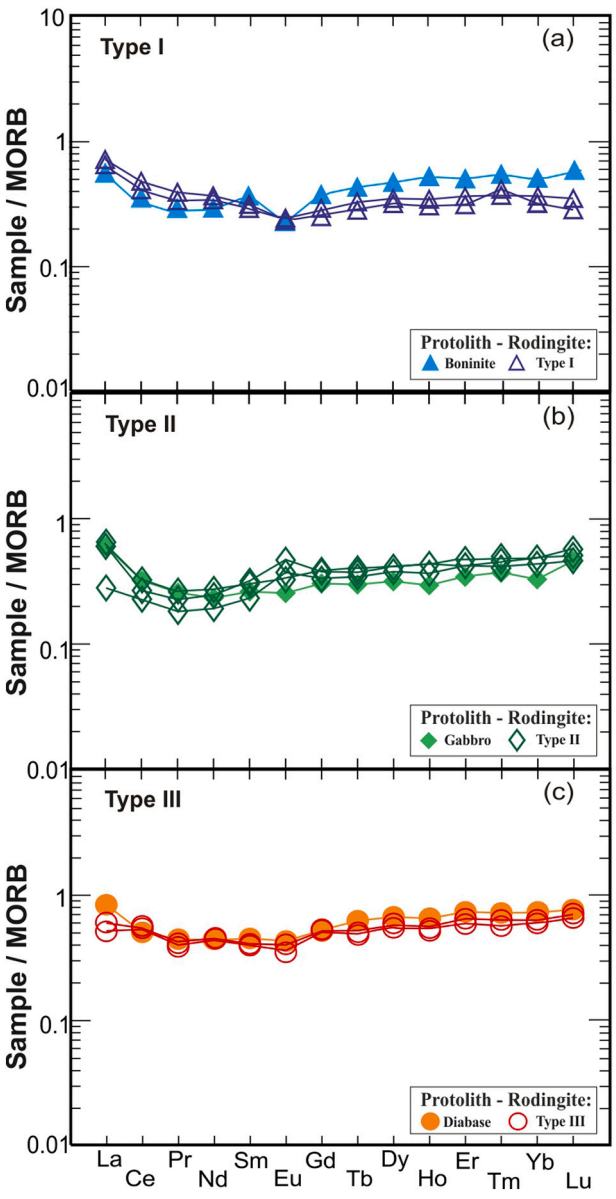

Fig. 7. MORB-normalised REE patterns of the Veria-Naousa rodingites and their protoliths: (a) Type I; (b) Type II and (c) Type III. Normalising values after McDonough and Sun (1995).

major and trace element abundances of unaltered and altered rocks can be plotted as variables, whereas the immobile elements form an isocon line. The reciprocal slope yields the total mass change during the rodingitisation, whereas the deviation of points above and below the isocon line illustrate the gains or losses of each component in the altered rock with respect to the protolith.

Fig. 8 displays the isocon plots of the various rodingite types (altered) and their precursors (unaltered rocks); the unaltered samples were collected in close proximity to the studied rodingite outcrops. Zr, Al and Ti are considered as relatively immobile elements during rodingitisation (Schandl et al., 1989; Dubińska, 1997; Li et al., 2007). Although these three elements are generally considered to behave as immobile during rodingisation, one of these three elements was nevertheless chosen as the one that would be considered to behave "ideally" as immobile so as to construct the isocon diagram, in order to study the mobility of the other elements. Due to the fact that we have identified three types of rodingites, we proceeded in choosing the element that seems to have behaved as the least immobile in all samples considered;

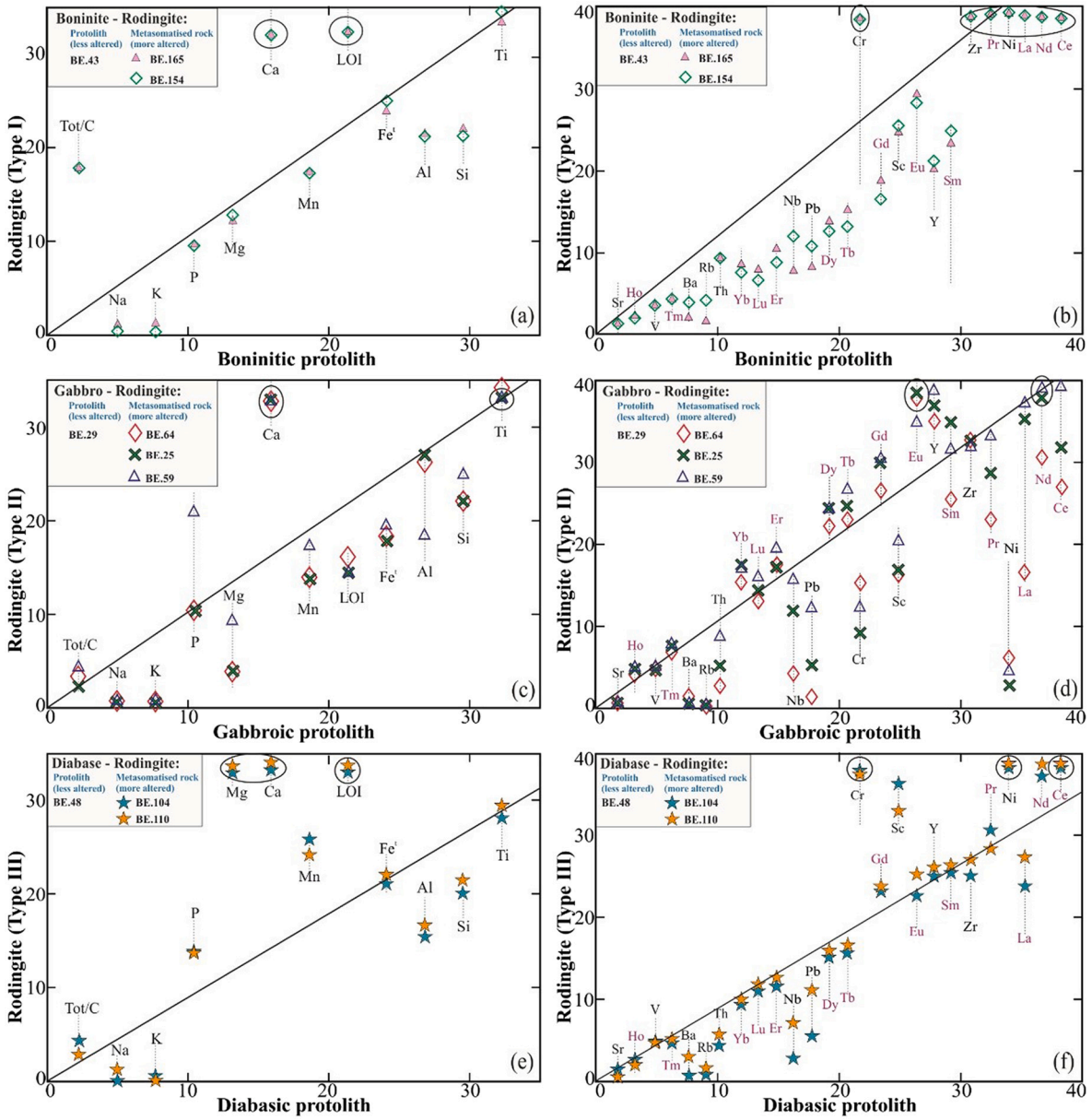

Fig. 8. Isocon plots using the method of Grant (1986) for major elements plotted as wt% of oxides [(a), (c), (e)] and for trace elements in ppm [(b), (d), (f)]. Solid lines represent constant Ti. Scaling factors for boninite, gabbro and diabase/rodingite pairs respectively are: SiO_2 (0.5, 0.6, 0.5), TiO_2 (146.6, 97.8, 46.1), Al_2O_3 (2.3, 1.9, 2.0), FeO_t (3.4, 2.3, 2.1), MnO (124.2, 116.4, 143.3), MgO (124.2, 1.5, 4.5), CaO (2.7, 2.3, 4.2), Na_2O (1.0, 7.4, 1.0), K_2O (29.6, 1.6, 30.8), P_2O_5 (521.7, 1043.5, 347.8), LOI (12.6, 5.8, 7.9), TOT/C (224.1, 112.1, 112.0), Ba (0.4, 0.002, 0.2), Sr (0.04, 0.002, 0.02), Y (2.1, 3.2, 1.7), Sc (0.8, 0.6, 0.7), Zr (2.7, 2.8, 1.1), Cr (0.05, 0.07, 1.6), Ni (0.7, 0.2, 1.3), Rb (3.4, 0.1, 2.9), Th (1020.6, 51.0, 14.6), V (0.03, 0.02, 0.01), Nb (19.8, 39.5, 14.4), Pb (1.3, 1.8, 4.3), La (25.3, 23.6, 16.9), Ce (16.6, 15.9, 10.1), Pr (90.7, 96.0, 55.3), Nd (18, 18, 18), Sm (30,30,30), Eu (117.5, 103.9, 61.4), Gd (17.4, 21.6, 12.5), Tb (69.0, 100.1, 47.7), Dy (8.7, 12.9, 6.1), Ho (6.0, 10.6, 4.8), Er (9.6, 13.9, 6.6), Tm (24.0, 35.3, 18.2), Yb (7.7, 11.6, 5.2), Lu (50.0, 61.9, 37.2).

in our case this is Ti.

Based on results from this study, a quantitative estimation of element losses and gains between the three types of rodingites and their precursors is given in Table 2. Several sets of elements were treated together due to similar patterns of enrichment or depletion relative to the assumed protolith composition.

4.5.1. *Type I rodingites – boninite protoliths*

Fig. 8a and b illustrate isocon plots of Type I rodingites (altered rocks) in correlation with a representative boninitic diabase (original rocks). The isocon line of Type I rodingite regarding the boninitic diabase has a reciprocal ratio from 0.73 to 0.79, which implies a mass loss of 21–27% during rodingitisation (Fig. 8a, b). Observation of the isocon plots shows that besides the expected gain in Ca, all other major elements were depleted during the rodingitisation (Fig. 8a). Assuming that Ti remained immobile in the system, most of the trace elements were slightly removed, except for Cr and Ni, which were significantly enriched (see Table 8 and Fig. 8b). Regarding the REE, the LREE remained relatively immobile lying close to the isocon line (gains or losses are essentially with their analytical uncertainties), whereas the MREE and HREE were slightly depleted (Fig. 8b).

4.5.2. *Type II rodingites – gabbroic protoliths*

The isocon plots of Type II rodingites (Fig. 8c, d) are projected in correlation with a representative gabbroic rock considered as their protolith. An isocon line has been drawn based on the assumption of Ti immobility, resulting in a reciprocal ratio ranging from 0.85 to 0.94 and consequently with an average mass loss of ~10%. Calculated element

Table 2
Elemental gains (+) and losses (−) calculated using isocon method of Grant (1986, 2005), assuming constant TiO_2 for Veria-Naousa rodingites with respect to the protoliths.

Rodingite Type	Type I		Type II			Type III	
Constant	Ti		Ti			Ti	
Sample	BE.165	BE.154	BE.25	BE.59	BE.64	BE.104	BE.110
Major elements							
SiO_2	−41.15	−46.96	−31.83	−29.46	−29.31	−20.90	−19.94
TiO_2	+0.00	+0.00	+0.00	+0.00	+0.00	+0.00	+0.00
Al_2O_3	−36.90	−41.55	−8.14	−42.05	−7.61	−34.00	−31.27
$Fe_2O_3^t$	−17.80	−20.20	−32.28	−32.21	−28.14	+0.90	+0.16
MnO	−26.67	−31.56	−31.25	−15.38	−29.29	+58.89	+43.03
MgO	−13.54	−14.86	−71.97	−39.41	−72.15	+421.11	+318.02
CaO	+224.84	+198.32	+355.61	+267.35	+364.22	+193.22	+175.35
Na_2O	−99.68	−98.95	−98.63	−98.74	−98.59	−99.29	−66.64
K_2O	−96.98	−97.18	−99.81	−99.82	−99.80	−100.00	−95.63
P_2O_5	−21.43	−26.67	−8.33	+69.23	−5.71	+53.01	+45.83
LOI	+61.76	+89.80	−38.06	−42.83	−28.65	+138.01	+106.60
TOT/C	+528.57	+486.67	−8.33	+69.23	+41.43	+14.75	+9.37
Trace elements							
Cr	+60.33	+58.72	−96.32	−53.45	−37.86	+3154.10	+2056.25
Ni	+373.73	+378.53	−93.01	−88.83	−83.24	+624.76	+457.98
Sr	−57.35	−50.76	−99.57	−99.82	−99.65	−0.91	−1.27
Ba	−77.55	−61.59	−99.94	−99.94	−99.84	−88.89	−54.13
Rb	−87.91	−66.15	−99.24	−99.29	−99.69	−88.52	−78.13
Th	−21.43	−26.67	−54.17	−15.38	−100.00	−50.82	−37.50
Nb	−60.71	−45.00	−31.25	−15.38	−76.43	−79.14	−50.28
Sc	−23.88	−26.67	−39.63	−31.89	−40.21	+63.07	+41.04
Zr	+30.26	+21.58	−4.24	−7.83	−0.66	−12.17	−5.63
Y	−43.88	−45.41	+19.48	+16.94	+16.53	+3.35	+2.98
V	−16.10	−24.18	−6.40	−7.53	−4.12	+20.29	+13.77
Pb	−62.75	−54.37	−72.98	−39.43	−96.03	−62.70	−28.91
REE							
La	−10.20	−5.71	−8.33	−9.74	−56.00	−28.96	−21.88
Ce	+5.90	+14.78	−23.61	−11.86	−33.21	+20.79	+18.01
Pr	−1.79	+5.93	−19.12	−12.90	−33.45	+8.92	−1.75
Nd	−6.46	−5.71	−2.94	−0.45	−22.35	+14.75	+12.79
Sm	−38.27	−37.89	+11.59	−1.90	−15.28	+1.25	−0.74
Eu	−14.60	−23.48	+69.23	+10.65	+37.80	−3.50	+1.92
Gd	−38.95	−50.41	+13.76	+7.28	+3.55	+10.61	+7.12
Tb	−40.39	−51.95	+14.58	+14.23	+8.43	−9.84	−8.85
Dy	−41.53	−50.20	+20.95	+11.65	+12.62	−5.87	−5.99
Ho	−48.11	−57.11	+34.44	+24.10	+16.29	−4.37	−5.54
Er	−42.90	−54.53	+10.36	+15.83	+14.42	−7.25	−3.61
Tm	−46.57	−44.27	+13.24	+9.50	+5.38	−9.59	−3.88
Yb	−41.72	−52.41	+38.42	+25.23	+24.46	−5.92	−4.91
Lu	−51.65	−63.33	+0.40	+4.76	−5.71	−1.64	+0.00
Total mass gains or losses	−21%	−27%	−6%	−8%	−15%	+15%	+9%

losses and gains are displayed in Table 2. Amongst the major elements, Ca was the only phase that was significantly enriched (see Table 2 and Fig. 8a). Si, Fe, Mg and Mn were fairly depleted, whereas alkali elements were drastically reduced. Ni and Cr were significantly removed from the system (Fig. 8b). The isocon plots reveal Zr and V remained constant during the metasomatic process, Y was fairly enhanced, whereas all other trace elements were variably depleted. Regarding the REE, the LREE were slightly depleted, whereas MREE and HREE were moderately enriched (Table 2 and Fig. 8c).

4.5.3. *Type III rodingites – diabasic protoliths*

Fig. 8e and f illustrate isocon plots of Type III rodingites, with the relevant losses and gains being calculated assuming Ti immobility (Table 2). A mass increase of ~15% occurred during rodingitisation as calculated from the reciprocal ratio (1.15) for the isocon line. The isocon plots show that Ca, Mn, Mg and P have entered into the system, whereas Si, Al and alkalies were variably depleted (Fig. 8e) and Fe remained immobile. Sc, Ni and Cr contents were enhanced, wheraes Sr, Y and Zr remained essentially immobile (gains and losses are within analytical errors) (Fig. 8f). All other trace elements considered were variably reduced through rodingitisation. Isocon plot for REE in this type of rodingites shows that all REE remained essentially immobile lying near or close to the isocon line (Fig. 8f).

5. Discussion

5.1. *Rodingite protoliths and rodingitisation processes*

Field observations have shown that the precursor rocks of the studied rodigites were subjected to rodingitisation of variable intensity. The least metasomatically affected rocks are considered as the protoliths of the Veria-Naousa ophiolitic rodingites, which comprise of boninitic diabases, gabbros and tholeiitic diabases. The chemical composition of the studied rocks and their minerals in combination with their textural characteristics show a complex petrogenetic evolution for the rodingites of the Veria-Naousa ophiolite. Based upon detailed petrographic observations and geochemical data, three different types of rodingites have been identified. In particular, Type I rodingites mainly exhibit granoblastic and porphyroblastic textures, which are in accordance with those that are also observed in their boninitic protolith. Moreover, the presence of relict magnesiochromites with high Cr# (see § 4.3) suggest that they were likely inherited from a protolith of boninitic affinity. Furthermore, the chemistry of the relict clinopyroxene of Type of rodingites is highly comparable with those identified in the boninites;

medium grained sizes observed in both the rodingites and the protolith. Apart from textural and mineral chemistry observations, the high Cr and Ni contents of the Type I rodingites provide further support that these were most likely formed after rodingitization of a boninitic protolith; REE contents amongst the protolith and Type I rodingites are very similar.

Type II rodingites display mainly blastophitic to blastosubophitic textures that are comparable with the subophitic and ophitic textures noticed in the gabbro protolith. The former rodingites comprise of grossular garnet (medium to coarse grained see § 4.2) that in many cases pseudomorphically retain the shapes of the former magmatic plagioclase grains; in the case of the gabbroic protolith considered, the plagioclase crystals display comparable subhedral shapes and sizes. Regarding their geochemistry, it is observed that the gabbro protolith and the Type II rodingites exhibit highly comparable Ti, Al, Zr, V as well as REE contents. Concerning the Type III rodingites, they comprise of mineral constituents that are of smaller size (see § 4.2), displaying relic subophitic textures, which resemble those of a diabasic rock. The Ti, Fe, Y, Zr, V and REE contents between the Type III rodingites and the diabase protolith considered, can be regarded as very carable.

The protoliths were affected by restricted metasomatism, as shown from the presence of actinolite, epidote and/or chlorite and prehnite, partly replacing the primary magmatic mineral phases (Supplementary Table 1). Clinopyroxene, plagioclase and in some cases magmatic amphibole are considered as the main primary magmatic phases in the protoliths. Clinopyroxene within the boninitic diabase is classified as augite, whereas clinopyroxene included in gabbro and tholeiitic diabase is diopside or augite. Clinopyroxene from the boninitic diabase displays relatively higher Mg# values compared to those present within the other two protoliths. Plagioclase in the boninitic diabase is classified as albite, due to the effects of low-grade albitisation, whereas in the gabbro and the tholeiitic diabase it appears as albite, labradorite and andesine. Magmatic amphibole is present within the gabbro and to a smaller extent in the tholeiitic diabase as interstitial crystals and blebs, displaying lower silica and higher Ti, Al and Na contents compared to secondary amphiboles, such as tremolite and actinolite (Maeda et al., 2002; Koutsovitis and Magganas, 2016; Abu-Alam and Stüwe, 2009; Ridolfi et al., 2010). Based on the textural characteristics and the chemistry of amphiboles in the gabbros and tholeiitic diabasic rocks of our study, we consider that blebs and granular hornblende were crystallised during the main magmatic stage from a hydrous silicate melt, whereas fibrous amphibole (actinolite) formed at the expense of magmatic hornblende and clinopyroxene during the metasomatic stage.

Three distinctive rodingite mineralogical assemblages have been identified and include: garnet (grossular and minor andradite) + diopside + chlorite at Type I; garnet (grossular and minor andradite) + diopside + vesuvianite ± quartz at Type II; chlorite + vesuvianite + diopside + garnet (andradite and grossular) at Type III. The mineral abundances of chlorite, garnet and vesuvianite vary significantly amongst the three distinct mineralogical assembladges, suggesting that rodingitisation of the Veria-Naousa mafic rocks occurred at different stages and chemical reactions. Initiation of rodingitisation processes coincides with the formation of grossular, which is the predominant mineral phase in Type I and II rodingites, but which is also present in smaller amounts in the Type III (Supplementary Table 1). Formation of garnet was facilitated through the reaction of either clinopyroxene or amphibole in the protoliths along with plagioclase in the presence of water, according to reactions (1) and (2) of Frost and Beard (2007):

$$5\mathrm{Cpx} + 4\mathrm{An} + 8\ \mathrm{H_2O} \rightarrow 3\mathrm{Grs} + \mathrm{Chl} + 6\mathrm{SiO_2(aq)} \quad (1)$$

$$2\ \mathrm{Amp} + 5\mathrm{An} + 6\mathrm{H_2O} = 3\mathrm{Grs} + 2\mathrm{Chl} + 11\mathrm{SiO_2(aq)} \quad (2)$$

The development of grossular instead of hydrogrossular in the Veria-Naousa rodingites is likely associated with relatively higher silica activity and of enhanced CO_2/H_2O ratio values that promoted garnet crystallisation during the early stages of rodingitisation. Subsequent formation of secondary anhedral to subhedral diopside neoblasts occured at the expense of garnet with additional hydration, according to the following reaction of Li et al. (2008):

$$\mathrm{Grs} + \mathrm{Chl} + \mathrm{H_2O} \pm \mathrm{Cm} \rightarrow \mathrm{Di} + \mathrm{SiO_2(aq)} \quad (3)$$

where Cm symbolises mobile components, such as Ca, Na and Si.

Andradite is mainly present in the Type III rodingites that most likely developed during the second stage of rodingitisation. In particular, early stage grossular was replaced according to reaction (4) of Li et al. (2008) by andradite and chlorite, assisted by the interaction with low-CO_2, high-pH, Fe-rich and Ca-rich fluids (Mubarak et al., 2020). The stability field for the development of andradite is favoured at temperatures of ~300 °C, although it has been reported that it can also be formed at even lower temperatures of 200–250 °C (Buse et al., 2010; Beard and Hopkinson, 2000).

$$\mathrm{Grs} + \mathrm{Cpx\ (Di)} + \mathrm{H_2O} \pm \mathrm{Cm} \rightarrow \mathrm{Adr} + \mathrm{Chl} \quad (4)$$

The above reaction occurred during the late-stage crystallisation of andradite, which is supported by the fact that andradite appears at the rims of grossular grains in the Type III rodingites (Fig. 5f). The frequent association of vesuvianite with secondary diopside and garnet indicates that these minerals were involved in the final rodingitisation stage, and in particular, petrographic features show that vesuvianite formed after garnet (Fig. 5c, e, f). The following reactions (5–7) of Li et al. (2004, 2007, 2008) are provided to interpret the formation of vesuvianite in the Type II and III rodingites:

$$\mathrm{Grs} + \mathrm{Chl} + \mathrm{H_2O} \rightarrow \mathrm{Ves} \pm \mathrm{Cm} \quad (5)$$

$$\mathrm{Grs} + \mathrm{Chl} + \mathrm{Ca^{2+}} \rightarrow \mathrm{Ves} + \mathrm{H_2O} \quad (6)$$

$$\mathrm{Chl} + \mathrm{H_2O} \rightarrow \mathrm{Ves} \pm \mathrm{Di} \pm \mathrm{Cm} \quad (7)$$

Reactions (5) and (6) successfully interpret the occurrence of vesuvianite within the groundmass, whereas the presence of vesuvianite-rich veinlets that were developed along with diopside can be interpreted through reaction (7). Vesuvianite forms under the effects of water-rich and very CO_2-poor fluids at 300–350 °C temperature conditions (Rice, 1983), which are comparable with those given for the formation of andradite.

5.2. Chemical evolution of rodingitisation

Rodingitisation processes that affected the Veria-Naousa rodingites were modelled in the CFMASH system, using the winTWQ 2.3 software (Berman, 2007) (Fig. 9). Rodingitisation occurs at relatively low pressures estimated at 2–6 kbar (Li et al., 2007; Normand and Williams-Jones, 2007; Tsikouras et al., 2013; Koutsovitis et al., 2013). The mineralogical assembladges of the three rodingite types considered in this study are highly comparable with those mentioned in the aforementioned references and thus we consider similar pressure condition as appropriate for modelling. With respect to the initialy enhanced CO_2/H_2O ratios (see § 5.1), a X_{CO2} value of ~0.70 was chosen for modelling start up. The following reactions (8)–(11) provide information concerning the development of the rodingites mineral assembladges, which are projected on a T-XCO_2 diagram (Fig. 9):

$$2\mathrm{An} + 5\mathrm{Di} + 3\mathrm{H_2O} \rightarrow 2\mathrm{Grs} + \mathrm{Act} + \mathrm{Chl} + \mathrm{Prh} + 3\mathrm{SiO_{2(aq)}} \quad (8)$$

$$5\mathrm{Act} + \mathrm{Prh} \rightarrow 12\mathrm{Di_2} + \mathrm{Chl} + 2\mathrm{H_2O} \quad (9)$$

$$3\mathrm{An} + 2\ \mathrm{Amp} + 4\mathrm{H_2O} \rightarrow 2\mathrm{Grs} + 3\mathrm{Di_2} + \mathrm{Chl} + 7\mathrm{SiO_{2(aq)}} \quad (10)$$

$$5\ \mathrm{Amp} + \mathrm{An} \rightarrow 10\mathrm{Di_2} + \mathrm{Chl} + \mathrm{H_2O} \quad (11)$$

Depending on the type of rodingitisation process and the nature of the protoliths (boninitic diabases, gabbros and tholeiitic diabases), rodingitisation seems to have progressed in two separate reaction paths

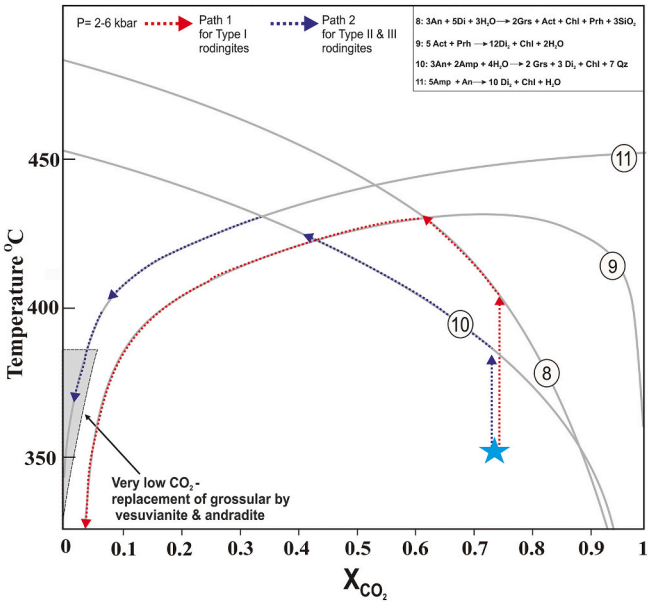

Fig. 9. T-X_{CO2} diagrams and possible path for evolution of the Veria-Naousa Type I, II and III rodingites; Abbreviations: An: anorthite, Amp: amphibole, Chl: chlorite, Di: diopside, Di_2: newly formed diopside, Grs: grossular, Act: actinolite, Prh; prehnite, Qz: quartz. The vesuvianite/andradite stability field is projected according to the Li et al. (2008) and Galuskin et al. (2003).

(p1) and (p2) (Fig. 9). The boninitic protoliths of Type I rodingites contained higher amounts of clinopyroxene compared to magmatic amphibole and thus we consider that these rocks were not vastly affected by reactions (10) and (11), but instead followed reactions (8) and (9), as shown by reaction path (p1) (Fig. 9). Reaction (8) marks the initial stage of rodingitisation accompanied by temperature increase. The scenario that rodingitisation was initially marked by increasing temperature conditions is attributed to the likelihood that when the mantle wedge ultramafics were intruded by the mafic protoliths they were only partly serpentinised. Therefore, it is highly likely that the serpentinized ultramafics density was not sufficient to cause buoyant upward movement (Karson, 2021), but instead were likely drifted at least to a certain extent by the downgoing slab. Reaction (9) occurred at a more mature phase, when the ultramafics became completely serpentinised and thus less dense, leading to their gradual exhumation. By applying the TWQ software, the calculated reaction path (p1) is initiated at temperatures of ~400 °C, primary mineral phases were mostly replaced by grossular, actinolite, chlorite and prehnite (reaction 8), corresponding to the first rodingitisation stage. At the second rodingitisation stage, with further decrease of CO_2, additional secondary diopside and chlorite were developed, as described by reaction (9). Formation of Type I rodingites through path (p1) is further supported by the fact that their mineralogical assemblage contains grossular, two types of clinopyroxene (relict and newly formed), and only minor amounts of andradite and chlorite, as observed through petrographic observations and XRPD analyses (see § 4.2.2, Supplementary Table 1). The projected pattern of reaction path (p1) in the T-XCO_2 diagram (Fig. 9), is Capable to produce only minor amounts of andradite and/or vesuvianite, which is confirmed through the petrographic and mineralogical observation (see § 5.1).

Type II and III rodingites were formed mainly by decomposition of magmatic amphibole that was retained in their protoliths. Based on the TWQ calculated reaction paths, rodingitisation was initiated at 380 °C, following the reaction path (p2) (Fig. 9). This reaction path involves the replacement of magmatic amphibole and anorthite initially with water-rich fluids and at relatively higher temperatures, as described by reactions (10) and (11), forming grossular, newly developed diopside, chlorite and minor quartz.

Type II and III rodingites comprise of relatively abundant vesuvianite and andradite that crystallised during the final stages of rodingitisation, with temperatures below ~360 °C, and under very low CO_2. Reaction path (p2) also explains the significant desilification and advanced rodingitisation noticed for the Type II and III rodingites. Formation of andradite is favoured under the effects of low-CO_2, high-pH, Fe-rich and Ca-rich fluids and tends to form at temperatures between 300 and 380 °C (Beard and Hopkinson, 2000; Buse et al., 2010).

5.3. *Element mobility and conditions of rodingitisation*

The vast majority of rodingites form from metasomatic reactions associated with serpentinisation of ultramafic rocks and the subsequent circulation of hydrous metasomatic fluids during their exhumation to the earth's surface (Coleman, 1967; Schandl et al., 1989; Dubińska et al., 2004; Tsikouras et al., 2009; Koutsovitis et al., 2013). Rodingites in the Veria-Naousa ophiolite are in sharp contact with serpentinites, suggesting a close relationship between serpentinisation and rodingitisation. These rodingites present considerable enrichments in Ca and Cr (except the Type II rodingites) and Mg depletions (Type I and II rodingites) (see § 4.4 and Table 1). The source of Ca and Cr enrichment is attributed to clinopyroxene, olivine and spinel breakdown in the host peridotites during serpentinisation (Coleman, 1967; Tsikouras et al., 2009; Koutsovitis et al., 2013). Ca may also be transferred as ($CaOH^+$) complexes through leaching processes from the serpentinised peridotite to rodingite (Bach and Klein, 2009; Tsikouras et al., 2009). Depletions in mobile elements that include Na, K, Rb, Ba, Sr and Nb are attributed to metasomatic consumption of plagioclase, clinopyroxene and magmatic amphibole of the protoliths.

Mg tends to be removed during the initial stages of rodingitisation that progressively increased due to the leverage effects of late-stage serpentinisation and rodingitisation phenomena, which favours the formation of andradite, vesuvianite and chlorite (Mittwede and Schandl, 1992; Li et al., 2007). Significant gains of Mg in the Type III rodingites are interpreted due to the relatively high abundance in chlorite. Although Al tends to remain relatively stable during rodingitisation (e.g. Schandl et al., 1989; Li et al., 2007), in the case of the Veria-Naousa rodingites, Al contents were decreased (Table 2, Fig. 8a, c, e). This is attributed to the lower Al contents of the garnets that replaced the An-rich plagioclase phases in the protoliths. Recent research studies (Deschamps et al., 2013; Kelley and Cottrell, 2009; Parkinson and Arculus, 1999; Li et al., 2020) provided constraints regarding the oxidising conditions within the mantle wedge. At the slab front beneath the arcs, the fluid flux derived from sediments, the oceanic crust and the subducted serpentinised lithosphere is released in relatively high amounts, resulting in achieving relatively high oxidising conditions (Kelley and Cottrell, 2009; Foden et al., 2018; Bénard et al., 2018; Li et al., 2020). At even shallower depths, the fluid flux tends to decrease (Li et al., 2020) and thus the oxidation state is expected to be more confined. This may interpret the depletion of Fe observed mostly in the Type II and to a lesser extent in the Type I rondigites relative to their protoliths, whereas the shallower formed Type III rodingites exhibit Fe contents that remained relatively stable compared to their protoliths (Table 2).

Zr often behaves as an immobile element although research studies suggest that extensive rodingitisation can contribute to its removal from the protoliths (Dubińska et al., 2004; Pomonis et al., 2008; Tsikouras et al., 2009, 2013; Koutsovitis et al., 2013). The mobility of Zr is enhanced by the effects of highly alkaline hydrous fluids, forming mobile complexes with ligands such as F^- and OH^- (Aja et al., 1995; Bröcker and Enders, 2001; Veyland et al., 2000; Hatzipanagiotou et al., 2003; Pomonis et al., 2008; Tsikouras et al., 2009, 2013; Koutsovitis et al., 2013). In the Veria-Naousa rodingites, Zr was fairly enriched in the Type I rodingites, which is likely associated with restricted modifications in the pH conditions and remained relatively stable in the other

two rodingite Types (II and III). Ti remained relatively immobile in all of the rodingite Types consistent with the prevalence of oxidising conditions within the mantle wedge (Beard and Hopkinson, 2000; Dubińska, 1997; Knauss et al., 2001).

Cr and Ni contents of Veria-Naousa rodingites behave as highly mobile elements, as shown in the isocon plots (see § 4.5, Fig. 8b, d, f), especially noticed in the Type III rodingites, which were likely related with the continuous serpentinisation of the surrounding ultramafics. This allowed the liberation of Cr and Ni from the serpentinites, which were transferred into the rodingites in the form of $Cr(OH)_3$ and $Ni(OH)_2$ (Aiuppa et al., 2000; Rai et al., 2007; Tsikouras et al., 2013). Formation of the aforementioned hydroxides are favoured under relatively high CO_2/H_2O ratio of the circulating fluids, which occur at the initial stages of metasomatism, due to the effects of fluids derived from metamorphic decarbonation of subducted marine sediments and/or mafic rocks (pressure conditions ~5 kbar); these gradually became more H_2O enriched at shallower depths (Collins et al., 2015; Cook-Kollars et al., 2014; Piccoli et al., 2016).

Relevant studies show that rodingitisation may either slightly affect the REE contents (Hatzipanagiotou and Tsikouras, 2001) or it may have a profound effect upon them (Koutsovitis et al., 2008; Tsikouras et al., 2009). The mobility of REE is highly influenced by the composition of the fluid phase and by the water: rock ratio. In cases that this ratio exceeds the value of 100, the REE tend to become more mobile (Gillis et al., 1992; Pomonis et al., 2008; Tsikouras et al., 2009, 2013). Another contributing factor is the increase of CO_2 and F levels in the fluid phase, especially at low pH conditions (Price et al., 1991; Tsikouras et al., 2009, 2013), although this can also occur even under more alkaline conditions (Michard, 1989). Ligands, such as CO_3^{2-}, OH^-, F^-, Cl^-, PO_4^{3-}, SO_4^{2-} can act to further facilitate REE mobility (Michard, 1989; Rolland et al., 2003; Pomonis et al., 2008; Tsikouras et al., 2009).

Compared to their protoliths, Type I rodingites display rather stable LREE and restricted depletions in the MREE and HREE (Table 2). This may be attributed to the breakdown of clinopyroxene and amphibole, which subsequently led to REE modifications. In the Type II rodingites, the LREE are slightly depleted, whereas MREE and HREE are fairly enriched. These features are likely associated with the fact that these rodingites comprise of rather high amounts of garnet grains compared to the other rodingites. It has been observed that some of the Type II rodingites include apatite; PO_4^{3-} ligands may have contributed to the mobility of REE (Byrne et al., 1991; Ayers and Watson, 1991). REE remained almost immobile in the Type III rodingites. This is likely attributed to the shallower level rodingitisation under low pH and decreasing amounts of CO_2. These conditions promoted the formation of andradite and vesuvianite instead of grossular (Supplementary Table 1), which possess lower REE contents compared to grossular-rich garnets (Halama et al., 2013). Amongst the rodingites considered in this study, Type II rodingites are the only ones that display noticeable Eu enrichments compared to their protoliths (Fig. 7b). Rodingites of this Type comprise the highest amounts of grossular, which may interpret the selective partitioning of divalent Eu in the Ca-site of garnet (Whitney and Olmsted, 1998; Bocchio et al., 2000; Van Westernen et al., 2000; Tsikouras et al., 2009, 2013).

5.4. Petrogenetic processes of Veria-Naousa protoliths and rodingites

The Veria-Naousa ophiolite was formed at supra-subduction zone (SSZ) settings and represents exhumed members of the fore-arc section (Rogkala et al., 2017). The mafic protoliths (including boninites) of the rodingites display relatively low Nb/Th (1.6–4.0) and rather high Th/Yb (0.20–0.32) ratio values that are consistent with arc-related rocks (Sun and McDonough, 1989; Pearce and Peate, 1995; Fang and Niu, 2003; Koutsovitis and Magganas, 2016). In addition, the very low-Ti contents of the relict clinopyroxene grains (Supplementary Table 2) further confirm the aforementioned geotectonic setting. Partial melting of the mantle wedge peridotites resulted in the formation of boninitic and basaltic magma that was incorporated within the adjacent to the slab serpentinites of the mantle wedge (Nikolaeva et al., 2008; Gerya, 2011; Koutsovitis et al., 2013; Tang et al., 2018). These mechanisms that resulted in the intrusion of these magmas (as dykes) into the serpentinites are closely associated with the fast circulating route of the magmas and their short distance to the slab and the mantle wedge serpentinised peridotites (Jadamec and Billen, 2010; Long and Wirth, 2013; Koutsovitis et al., 2013) (Fig. 10). The mafic intrusions were subsequently subjected to ongoing rodingitisation processes due to continuous serpentinisation of the surrounding ultramafics. The serpentinite-protolith-rodingite association was exhumed towards the fore-arc oceanic basin and the accretionary prism, facilitated by slab roll-back mechanisms and due to the increasing volume of the serpentinites (Dilek et al., 2007; Gerya, 2011). Apart from the exhumed serpentinites and their incorporated rodingites, the Veria-Naousa ophiolite also consists of other less volumous serpentinised ultramafic rocks (cpx-harzburgite and lherzolite), pyroxenites and mafic rocks (Rogkala et al., 2017).

Rodingitisation took place in two distinct stages at fore-arc settings, which was aided by the slab derived fluids released after devolatilisation of the subducted sediments. These fluids contributed to the serpentinisation of mantle wedge peridotites, which facilitated rodingitisation processes upon the intrusive mafic rocks. The first stage was initiated under reducing pH and mildly oxidising conditions, at relatively elevated CO_2/H_2O ratios (see § 5.3). This stage affected the protoliths of all rodingite types, mainly forming grossular, chlorite and newly formed diopside, and in some cases (Type I rodingites) prehnite and actinolite, at the expense of plagioclase, clinopyroxene and magmatic amphibole. In the Type I rodingites grossular replaced most of the initial plagioclase, whereas chlorite formed at the expence of primary clinopyroxene. Protoliths of the Type II and III rodingites were subjected to further rodingitisation under lower CO_2/H_2O ratios, related with the smaller clinopyroxene/amphibole ratio of their protoliths and due to consumption of the hydrous magmatic phases. The second rodingitisation stage affected Type II and III rodingites affected by H_2O-rich fluids and lower temperature conditions at shallower depths, leading to the formation of andradite, vesuvianite and chlorite.

6. Conclusions

This study reports the occurrence of rodingitised dykes within serpentinites in the Veria-Naousa ophiolite. Based upon their metasomatic mineralogical assemblages, they are divided into three types: a) Rodingites derived from boninitic diabasic protoliths with garnet + clinopyroxene + chlorite + spinel (Type I), b) from gabbroic protolith with clinopyroxene + garnet + vesuvianite ± quartz (Type II) and c) diabasic tholeiitic protolith with grossularitic garnet + andraditic garnet + vesuvianite + clinopyroxene + chlorite (Type III). During the maturing stage of the arc and with progressive exhumation, mafic rocks hosted within serpentinised peridotites were affected by circulation of subduction-related metasomatic fluids forming rodingites.

Isocon analyses between rodingites and their protoliths showed that rodingitisation essentially occurred with Ti preservation. Rodingitisation resulted in desilification, decrease of alkalies, as well as Ca enrichment. Relative to the protoliths Cr and Ni were increased (expect Type II rodingites), whereas Al, Mg (except Type III rodingites) and Fe (except Type I rodingites) were variably depleted. The depletion of Fe in Type II rodingites is interpreted by the relatively intense oxidising conditions at deeper parts, whereas the shallower formed Type III rodingites exhibit stable Fe. Regarding the REE, Type I rodingites display rather stable LREE and restricted depletions in MREE and HREE, as the result of primary clinopyroxene breakdown. In the case of Type II rodingites, the LREE were slightly depleted in contrast to the MREE and HREE that were fairly enriched. This is attributed to the complete breakdown of plagioclase and magmatic amphibole from the gabbroic precursor and the development of rather high amounts of garnet

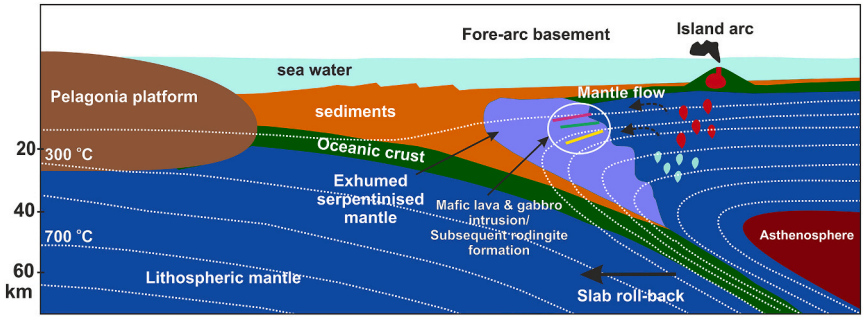

Fig. 10. Schematic profile of a fore-arc section in a supra-subduction zone (SSZ) setting, illustrating the exhumation model, which explains the formation of the Veria-Naousa rodingites. Rectangles indicate possible localities of rodingitisation and dotted arrows the mantle flow (yellow bar: gabbro, red bar: tholeiitic diabase, green bar: boninite). (For interpretation of the references to colour in this figure legend, the reader is referred to the web version of this article.)

compared to the other two types. The restricted mobility of REE in the Type III rodingites is attributed to shallow level late-stage rodingitisation under decreasing pH and decreasing amounts of CO_2. The latter conditions promoted the formation of andradite and vesuvianite instead of grossular.

The petrological data of this study show that the studied rodingites and their protoliths were formed at fore-arc settings, representing exhumed members developed close to the slab and facilitated by slab slab-roll back mechanisms due to the increasing volume of serpentinites. Rodingitisation took place in two distinct stages. The first stage was initiated under reducing pH and mildly oxidising conditions with increased CO_2/H_2O ratios, which resulted in the formation of grossular, chlorite and clinopyroxene neoblasts at the expense of plagioclase, clinopyroxene and amphibole. The second stage corresponds to the main rodingitisation phase, under more oxidising conditions with decreasing CO_2/H_2O ratios. In Type I rodingites, grossular replaced most of the initial plagioclase, whereas chlorite replaced most of the primary clinopyroxene and magmatic amphibole. Protoliths of Type II and III rodingites were subjected to further rodingitisation under progressively lower CO_2/H_2O ratio values. At the last stage of rodingitisation only Type II and III were affected, forming late-stage andradite and vesuvianite under very low CO_2/H_2O ratios and lower temperature conditions at shallower depths. All stages of rodingitisation are estimated to have occurred under relatively moderate temperature and pressure conditions (~300 to 450 °C; 2–6 kbar respectively).

Supplementary data to this article can be found online at https://doi.org/10.1016/j.chemer.2021.125860.

Declaration of competing interest

The authors declare that they have no known competing financial interests or personal relationships that could have appeared to influence the work reported in this paper.

Acknowledgements

We kindly thank Dr. A.K. Seferlis of the Laboratory of Electron Microscopy and Microanalysis, University of Patras for his assistance with the microanalyses and SEM micrographs. We kindly thank Dr. B. Tsikoura for his assistance in the fieldwork, in the interpretation of the results and for his whole contribution of this study. We also thank M. Kalpogiannaki for her assistance in the construction of the geological map. Finally, we also thank Ms. N. Zaronikola for her participation in the data curation. A. Rogkala was supported by the State Scolarship Foundation of Greece (IKY) during this research. This research is co-financed by Greece and the European Union (European Social Fund- ESF) through the Operational Programme «Human Resources Development, Education and Lifelong Learning» in the context of the project "Reinforcement of Postdoctoral Researchers - 2 nd Cycle" (MIS-5033021), implemented by the State Scholarships Foundation (IKY).

References

Abu-Alam, T.S., Stüwe, K., 2009. Exhumation during oblique transpression: the Feiran-Solaf region, Egypt. J. Metamorph. Geol. 27, 439–459.
Aiuppa, A., Allard, P., D'Alessandro, W., Michel, A., Parello, F., Treuil, M., Valenza, M., 2000. Mobility and fluxes of major, minor and trace metals during basalt weathering and groundwater transport at mt. Etna volcano (Sicily). Geochim. Cosmochim. Acta 64, 1827–1841.
Aja, S.U., Wood, S.A., Williams-Jones, A.E., 1995. The aqueous geochemistry and the solubility of some zr-bearing minerals. Appl. Geochem. 10, 603–620.
Ayers, J.C., Watson, E.B., 1991. Solubility of apatite, monazite, zircon, and rutile in supercritical aqueous fluids with implications for subduction zone geochemistry. Phil. Trans. R. Soc. A 335, 365–375.
Bach, W., Klein, F., 2009. The petrology of seafloor rodingites: insights from geochemical reaction path modelling. Lithos 112, 103–117.
Baltatzis, E., 1984. A new occurrence of rodingite from Skiros Island, Greece. Neues Jb. Mineral. Abh. 7, 317–322.
Beard, J.S., Hopkinson, L., 2000. A fossil, serpentinization-related hydrothermal vent, ocean drilling program leg 173, site 1068 (Iberia abyssal Plain): some aspects of mineral and fluid chemistry. J. Geophys. Res. 105, 16527–16539.
Bénard, A., Woodlandc, A.B., Arculusa, R.J., Nebelb, O., McAlpinea, S.R.B., 2018. Variation in sub-arc mantle oxygen fugacity during partial melting recorded in refractory peridotite xenoliths from the West Bismarck arc. Chem. Geol. 486, 16–30.
Berman, R.G., 2007. winTWQ (version 2.3): a software package for performing internally-consistent thermobarometric calculations. GSC Open Fille 5462.
Bish, D.L., Post, J.E., 1993. Quantitative mineralogical analysis using the rietveld full pattern fitting method. Am. Mineral. 78, 932–940.
Bocchio, R., De Capitani, L., Ottolini, L., Cella, F., 2000. Trace element distribution in eclogites and their clinopyroxene/garnet pair: a case study from soazza (Switzerland). Eur. J. Mineral. 12, 147–161.
Bröcker, M., Enders, M., 2001. Unusual bulk-rock compositions in eclogite-facies rocks from syros and tinos (Cyclades, Greece): implications for U-pb zircon geochronology. Chem. Geol. 175, 581–603.
Buse, B., Schumacher, J., Sparks, R., Field, M., 2010. Growth of bultfonteinite and hydrogarnet in metasomatized basalt xenoliths in the B/K9 kimberlite, damtshaa, Botswana: insights into hydrothermal metamorphism in kimberlite pipes. Contrib. Mineral. Petrol. 160, 533–550.
Byrne, R.H., Lee, J.H., Bingler, L.S., 1991. Rare earth element complexation by PO43– ions in aqueous solution. Geochim. Cosmochim. Acta 55, 2729–2735.
Capedri, S., Garuti, G., Rossi, S., 1978. Rodingites from pindos. Constrains on the "rodingite problem". Neues Jb. Mineral. Abh. 132, 242–263.
Coleman, R.G., 1967. Low-temperature reaction zones and alpine ultramafic rocks of California, Oregon, and Washington. U.S. Geol. Surv. Bull. 1247, 49p.
Coleman, R.G., 1977. Ophiolites: Ancient Oceanic Lithosphere? Springer-Verlag, Berlin, Germany.
Collins, N.C., Bebout, G.E., Angiboust, S., Agard, P., Scambelluri, M., Crispini, L., John, T., 2015. Subduction zone metamorphic pathway for deep carbon cycling: II. Evidence from HP/UHP metabasaltic rocks and ophicarbonates. Chem. Geol. 412, 132–150.
Cook-Kollars, J., Bebout, G.E., Collins, N.C., Angiboust, S., Agard, P., 2014. Subduction zone metamorphic pathway for deep carbon cycling: I. Evidence from HP/UHP metasedimentary rocks, Italian Alps. Chem. Geol. 386, 31–48.
Deschamps, F., Godard, M., Guillot, S., Hattori, K., 2013. Geochemistry of subduction zone serpentinites: a review. Lithos 178, 96–127.
Dilek, Y., Furnes, H., Shallo, M., 2007. Suprasubduction zone ophiolite formation along the periphery of mesozoic Gondwana. Gondwana Res. 11, 453–475.
Duan, W.-Y., Li, X.-P., Wang, Z.-L., Chen, S., Sun, G.-M., Zhao, L.-Q., 2021a. Thermodynamic modeling and elemental migration for the early stage of rodingitization: an example from the xialu massif of the xigaze ophiolite, southern Tibet. Geosci. Front. 12, 101125 https://doi.org/10.1016/j.gsf.2020.12.006.
Duan, W.-Y., Li, X.-P., Schertl, H.-P., Willner, A.P., Wang, S.-J., Chen, S., Sun, G.-M., 2021. Rodingitization records from ocean-floor to high pressure metamorphism in

the Xigaze ophiolite, southern Tibet. Gondwana Res. https://doi.org/10.1016/j.gr.2021.05.013 xxx (xxxx) xxx.
Dubińska, E., 1997. Rodingites and amphibolites from the serpentinites surrounding Göry sowie block (Lower Silesia, Poland): record of supra-subduction zone magmatism and serpentinization. Neues Jb. Mineral. Abh. 171, 239–279.
Dubińska, E., Bylina, P., Kozlowski, A., Dörr, W., Nejbert, K., Schastok, J., Kulicki, C., 2004. U-pb dating of serpentinization: hydrothermal zircon from a metasomatic rodingite shell (Sudetic ophiolite, SW Poland). Chem. Geol. 203, 183–203.
Economou, M., 1983. A short note on the evolution of the vermion ophiolite complex (Macedonia-Greece). Ofioliti 8, 333–338.
Economou-Eliopoulos, M., 2003. Apatite and mn. Zn. Co-enriched chromite in ni-laterites of northern Greece and their genetic significance. J. Geochem. Explor. 80, 41–54.
Evans, B.W., 1977. Metamorphism of alpine peridotite and serpentinite. Annu. Rev. Earth Planet. Sci. 5, 397–447.
Fang, N., Niu, Y., 2003. Late palaeozoic ultramafic lavas in Yunnan, SW China, and their geodynamic significance. J. Petrol. 44, 141–158.
Fitzgerald, S., Leavens, P.B., Nelen, J.A., 1992. Chemical variation in vesuvianite. Mineral. Petrol. 46, 163–178.
Foden, J., Sossi, P.A., Nebel, O., 2018. Controls on the iron isotopic composition of global arc magmas. Earth Planet. Sci. Lett. 494, 190–201.
Frost, B.R., 1975. Contact metamorphism of serpentinite, chloritic blackwall and rodingite at Paddy-Go-Easy Pass, central Cascades, Washington. J. Petrol. 16, 272–313.
Frost, B.R., Beard, J.S., 2007. On silica activity and serpentinization. J. Petrol. 48, 1351–1368.
Frost, B.R., Beard, J.S., Caig, A.M.C., Condliffe, E., 2008. In: The Formation of Micro-Rodingites From IODP Hole U1309D : KeyT o Understanding the Process of Serpentinization, 49(9), pp. 1579–1588.
Fukuyama, M., Ogasawara, M., Dunkley, D.J., Wang, K., Lee, D., Hokada, T., Maki, K., Hirata, T., Kon, Y., 2014. The formation of rodingite in the Nagasaki metamorphic rocks at nomo peninsula, Kyushu, Japan – zircon U-pb and hf isotopes and trace element evidence. Island Arc 23, 281–298.
Galuskin, E.V., Armbruster, T., Malsy, A., Galuskina, I.O., Sitarz, M., 2003. Morphology, composition and structure of low-temperature P4/nnc high-fluorine vesuvianitewhiskers from Polar Yakutia, Russia. Can. Mineral. 41, 843–856.
Gerya, T.V., 2011. Intra-oceanic subduction zones. In: Brown, D., Ryan, P.D. (Eds.), Arccontinent Collision, Frontiers in Earth Sciences. Springer-Verlag, Berlin Heidelberg, pp. 23–51.
Gillis, K.M., Ludden, J.N., Smith, A.D., 1992. Mobilization of the REE during crustal aging in the Troodos ophiolite, Cyprus. Chem. Geol. 98, 71–86.
Grant, J.A., 1986. The isocon diagram — a simple solution to Gresens' equation for metasomatic alteration. Econ. Geol. 81, 1976–1982.
Grant, J.A., 2005. Isocon analysis: a brief review of the method and applications. Phys. Chem. Earth Parts A/B/C 30, 997–1004.
Grew, E.S., Locock, A.J., Mills, S.J., Galuskina, I.O., Galuskin, E.V., Hålenius, U., 2013. IMA report nomenclature of the garnet supergroup. Am. Mineral. 98 (4), 785–811.
Halama, R., Savov, I.P., Garbe-Scönbergi, D., Schenk, V., Toulkeridis, T., 2013. Vesuvianite in high-pressure-metamorphosed oceanic lithosphere (Raspas complex, Ecuador) and its role for transport of water and trace elements in subduction zones. Eur. J. Mineral. 25, 193–219.
Hatzipanagiotou, K., Tsikouras, B., 2001. Rodingite formation from diorite in the Samothraki ophiolite, NE Aegean, Greece. Geol. J. 36 (2), 93–109.
Hatzipanagiotou, K., Tsikouras, B., Migiros, G., Gartzos, E., Serelis, K., 2003. Origin of rodingites in ultramafic rocks from Lesvos Island (NE Aegean, Greece). Ofioliti 28 (1), 13–23.
Hernández-Uribe, D., Palin, R.M., Cone, K.A., Cao, W., 2020. Petrological implications of seafloor hydrothermal alteration of subducted mid-ocean ridge basalt. J. Petrol. 61 (9), egaa086.
Hey, M.H., 1954. A review on the chlorites. Mineral. Mag. 224, 277–298.
Jadamec, M., Billen, M.I., 2010. Reconciling rapid 3-D mantle flow and surface plate motions near the eastern Alaska slab edge. Nature 465, 338–341.
Karkalis, C., Magganas, A., Koutsovitis, P., 2019. Petrological and geochemical comparison of rodingites from Kimi -evia island with outcrops from adjacent regions. Bull. Geol. Soc. Greece 54, 1–19.
Karkalis, C., Magganas, A., Koutsovitis, P., Pomonis, P., Ntaflos, T., 2021. Multiple rodingitization stages in alkaline, tholeiitic and calc-alkaline basaltic dikes intruding exhumed serpentinized Tethyan mantle from Evia Island, Greece. Lithosphere. https://doi.org/10.2113/2021/9507697.
Karson, J.A., 2021. Oceanic transform faults. In: Encyclopedia of Geology, Second edition, pp. 930–946.
Kelley, K.A., Cottrell, E., 2009. Water and oxidation state of subduction zone magmas. Science 325, 605–607.
Knauss, K.G., Johnson, J.W., Steefel, C.I., Nitao, J.J., 2001. In: Proceedings of the 1st National Conference on Carbon Sequestration (May 14-17, Washington DC), Evaluation of the Impact of CO2, Aqueous Fluid, and Reservoir Rock Interactions on the Geologic Sequestration of CO2, With Special Emphasis on Economic Implications (DOE National Energy Technology Laboratory), p. 11.
Koutsovitis, P., Magganas, A., 2016. Boninitic and tholeiitic basaltic lavas and dikes from dispersed jurassic east othris ophiolitic units, Greece: petrogenesis and geodynamic implications. Int. Geol. Rev. 58 (16), 1983–2006.
Koutsovitis, P., Magganas, A., Pomonis, P., 2008. Rodingites within scattered ophiolitic occurrences from the northern and eastern Orthis area, Greece. In: Proceedings of the 13th International Conference on Thermobarogeochemistry and IVth APIFIS Symposium, 1, pp. 243–246.
Koutsovitis, P., Magganas, A., Pomonis, P., Ntaflos, T., 2013. Subduction-related rodingites from east othris, Greece: mineral reactions and physicochemical conditions of formation. Lithos 172–173, 139–157.
Koutsovitis, P., Magganas, A., Ntaflos, T., Koukouzas, N., 2018. Rodingitization and carbonation, associated with serpentinization of triassic ultramafic cumulates and lavas in othris, Greece. Lithos 320–321, 35–48.
Le Bas, M.J., 2000. IUGS reclassification of the high-mg and picritic volcanic rocks. J. Petrol. 41, 1467–1470.
Leake, B.E., Woolley, A.R., Arps, C.E.S., Birch, W.D., Gilbert, M.C., Grice, J.D., Hawthorne, F.C., Kato, A., Mandarino, J.A., Maresch, W.V., Nickel, E.H., Rock, N.M.S., Schumacher, J.C., Smith, D.C., Stephenson, N.C.N., Ungaretti, L., Whittaker, E.J.W., Youzhi, G., 1997. Nomenclature of amphiboles: report of the subcommittee on amphiboles of the international mineralogical association, commission on new minerals and mineral names. Am. Mineral. 82, 1019–1037.
Li, X.P., Rahn, M., Bucher, K., 2004. Metamorphic processes of rodingites of the Zermatt-saas ophiolites, Central Alps. Int. Geol. Rev. 46, 28–51.
Li, X.-P., Zhang, L.-F., Wei, C.-J., Ai, Y.-L., Chen, J., 2007. Petrology of rodingite derived fromeclogite in western Tianshan, China. J. Metamorph. Geol. 25, 363–382.
Li, X.P., Zhang, L.F., Wang, Z.L., 2008. Geochemistry of rodingite derived from eclogite in western Tianshan, China. Acta Petrol. Sin. 24 (4), 711–717.
Li, X.P., Zhang, L.F., Wilde, S.A., Song, B., Liu, X.M., 2010. Zircons from rodingite in the Western tianshan serpentinite complex: mineral chemistry and U-pb ages define nature and timing of rodingitization. Lithos 118 (1–2), 17–34.
Li, X.P., Duan, W.Y., Zhao, L.Q., Schertl, H.P., Kong, F.M., Shi, T.Q., Zhang, X., 2017. Rodingites from the xigaze ophoiolite, southern Tibet - new insights into the processes of rodingitization. Eur. J. Mineral. 29, 821–837.
Li, J.L., Schwarzenbach, E.M., John, T., Ague, J.J., Huang, F., Gao, J., Klemd, R., Whitehouse, M.J., Wang, X.S., 2020. Uncovering and quantifying the subduction zone sulfur cycle from the slab perspective. Nat. Commun. 11 (1), 514.
Long, M.D., Wirth, E.A., 2013. Mantle flow in subduction systems: the mantle wedge flow field and implications for wedge processes. J. Geophys. Res. Solid Earth 118, 583–606.
Maeda, J., Naslund, H.R., Jang, Y.D., Kikawa, Eiichi, Tajima, Takahiro, Blackburn, W.H., 2002. Geochemical Composition and Crystallization Temperatures of ODP Hole 176-735B Gabbroic Rocks. PANGAEA.
McDonough, W.F., Sun, S.S., 1995. The composition of the earth. Chem. Geol. 120, 223–253.
Mercier, J., Vergely, P., Bebien, J., 1975. Les ophiolites hélleniques “obductées” au jurassique supérieur sont-elles les vestiges d’ un océan tethysienou d’ Une mer marginale péri-européenne. Bull. Soc. Geol. Fr. 17, 108–112.
Michailidis, K.M., 1990. Zoned chromites with high mn-contents in the fe-ni-cr-laterite ore deposits from the Edessa area in northern Greece. Miner. Depos. 25, 190–197.
Michard, A., 1989. Rare earth element systematics in hydrothermal fluids. Geochim. Cosmochim. Acta 53, 745–750.
Mittwede, S.K., Schandl, E.S., 1992. Rodingites from the southern Appalachian Piedmont, South Carolina, USA. Eur. J. Mineral. 4 (1), 7–16.
Morimoto, N., 1988. Nomenclature of pyroxenes. Mineral. Petrol. 39, 55–76.
Mubarak, H.S., Azer, M.K., Surour, A.A., Mousa, H.E., Asimow, P.D., Kabesh, M.M.L., 2020. Mineralogical and geochemical study of rodingites and associated serpentinized peridotite, Eastern Desert of Egypt, Arabian-Nubian Shield. Lithos 105720, 374–375.
Nikolaeva, K., Gerya, T.V., Connolly, J.A.D., 2008. Numerical modelling of crustal growth in intraoceanic volcanic arcs. Phys. Earth Planet. Inter. 171, 336–356.
Normand, C., Williams-Jones, A.E., 2007. Physicochemical conditions and timing of rodingite formation: evidence from rodingite-hosted fluid inclusions in the JM Asbestos mine, Asbestos, Québec. Geochem. Trans. 8, 11.
Parkinson, I.J., Arculus, R.J., 1999. The redox state of subduction zones: insights from arc-peridotites. Chem. Geol. 160, 409–423.
Pearce, J.A., Peate, D.W., 1995. Tectonic implications of the composition of volcanic ARC magmas. Annu. Rev. Earth Planet. Sci. 23, 251–285.
Perraki, M., Karipi, S., Rigopoulos, I., Tsikouras, B., Pomonis, P., Hatzipanagiotou, K., 2010. Grossular/Hydrogrossular in rodingites from Othrys ophiolite (Central Greece): Raman spectroscopy as a tool to distinguish from vesuvianite. In: Scientific Annals of the School of Geology, Aristotle University of Thessaloniki, Special Volume 99, 317 – 322, Proceedings of the XIX CBGA Congress, Thessaloniki, Greece, 23 – 26/9/2010.
Piccoli, F., Brovarone, A.V., Beyssac, O., Martinez, I., Ague, J.J., Chaduteau, C., 2016. Carbonation by fluid–rock interactions at high-pressure conditions: implications for carbon cycling in subduction zones. Earth Planet. Sci. Lett. 445, 146–159.
Pomonis, P., Tsikouras, B., Karipi, S., Hatzipanagiotou, K., 2008. Rodingite formation in ultramafic rocks from the koziakas ophiolite, western Thessaly, Greece: conditions of metasomatic alteration, geochemical exchanges and T-X(CO2) evolutionary path. Can. Mineral. 46 (3), 569–581.
Price, R.C., Gray, C.M., Wilson, R.E., Frey, F.A., Taylor, S.R., 1991. The effects of weathering on rare-earth element evidence. Chem. Geol. 93, 245–265.
Rai, D., Moore, D.A., Hess, N.J., Rosso, K.M., Rao, L., Heald, S.M., 2007. Chromium(III) hydroxidesolubility in the aqueous K+–H+–OH−–CO2–HCO3−–CO32−–H2O system: a thermodynamic model. J. Solut. Chem. 36, 1261–1285.
Rice, J.M., 1983. Metamorphism of rodingites: part I. Phase relations in a portion of the system CaO-MgO-Al2O3-SiO2-CO2-H2O. Am. J. Sci. 283-A, 121–150.
Ridolfi, F., Renzulli, A., Puerini, M., 2010. Stability and chemical equilibrium of amphibole in calc-alkaline magmas: an overview, new thermobarometric formulations and application to subduction-related volcanoes. Contrib. Mineral. Petrol. 160, 45–66.

Rogkala, A., Petrounias, P., Tsikouras, B., Hatzipanagiotou, K., 2017. New occurrence of pyroxenites in the Veria-Naousa ophiolite (north Greece): implications on their origin and petrogenetic evolution. Geosciences 7, 92.
Rogkala, A., Petrounias, P., Tsikouras, B., Giannakopoulou, P.P., Hatzipanagiotou, K., 2019. Mineralogical evidence for partial melting and melt-rock interaction processes in the mantle peridotites of Edessa ophiolite (north Greece). Minerals 9 (2), 120.
Rolland, Y., Cox, S., Boullier, A.-M., Pennacchioni, G., Mancktelow, N., 2003. Rare earth and trace element mobility in mid-crustal shear zones: insights from the Mont Blanc massif (Western Alps). Earth Planet. Sci. Lett. 214, 203–219.
Saccani, E., Photiades, A., Santato, A., Zeda, O., 2008. New evidence for supra-subduction zone ophiolites in the vardar zone of northern Greece: implications for the tectono-magmatic evolution of the vardar oceanic basin. Ofioliti 33 (1), 65–85.
Salvioli-Mariani, E., Boschetti, T., Toscani, L., Montanini, A., Petriglieri, J.R., Bersani, D., 2020. Multi-stage rodingitization of ophiolitic bodies from northern apennines (Italy): constraints from petrography, geochemistry and thermodynamic modelling. Geosci. Front. 11, 2103–2125.
Schandl, E.S., O'Hanley, D.S., Wicks, F.J., 1989. Rodingites in serpentinized ultramafic rocks of the Abiti greenstone belt, Ontario. Can. Mineral. 579–591.
Serelis, K., 1995. In: Investigation of the Southern Lesvos Ophiolite. Agricultural University of Athens, pp. 1–238 (PhD Thesis).
Shen, T.T., Wu, F.Y., Zhang, L.F., Hermann, J., Li, X.P., Du, J.X., 2016. In-situ U-Pb dating and isotopic analysis of perovskite from a rodingite blackwall associated with UHP serpentinite from southwestern Tianshan, China. Chem. Geol. 431, 67–82.
Sideridis, A., Zaccarini, F., Koutsovitis, P., Grammatikopoulos, T., Tsikouras, B., Garuti, G., Hatzipanagiotou, K., 2021. Chromitites from the Vavdos ophiolite (Chalkidiki, Greece): petrogenesis and geotectonic settings; constrains from spinel, olivine composition, PGE mineralogy and geochemistry. Ore Geol. Rev. 137 https://doi.org/10.1016/j.oregeorev.2021.104289.
Sun, S.S., McDonough, W.F., 1989. Chemical and isotopic systematics of oceanic basalts: implications for mantle composition and processes. In: Saunders, A.D., Norry, M.J. (Eds.), Magmatism in the Ocean Basins: Geological Society London Special Publications, 42, pp. 313–345. In press.
Tang, Y., Zhai, Q.G., Hu, P.Y., Wang, J., Xiao, X.C., Wang, H.T., Tang, S.H., Lei, M., 2018. Rodingite from the beila ophiolite in the bangong-nujiang suture zone, northern Tibet: new insights into the formation of ophiolite related rodingite. Lithos 316–317, 33–47.
Tsikouras, B., Rigopoulos, I., Perraki, M., 2009. Geochemical processes and petrogenetic evolution of rodingite dykes in the ophiolite complex of othrys (Central Greece). Lithos 113, 540–554.
Tsikouras, B., Karipi, S., Hatzipanagiotou, K., 2013. Evolution of rodingites along stratigraphic depth in the iti and kallidromon ophiolites (Central Greece). Lithos 175–176, 16–29.
Tsoupas, G., Economou-Eliopoulos, M., 2008. High PGE contents and extremely abundant PGE-minerals hosted in chromitites from the Veria ophiolite complex. Northern Greece. Ore Geol. Rev. 33, 3–19.
Umino, S., Kitamura, K., Kanayama, K., Tamura, A., Sakamoto, N., Ishizuka, O., Arai, S., 2015. Thermal and chemical evolution of the subarc mantle revealed by spinel-hosted melt inclusions in boninite from the ogasawara (Bonin) archipelago, Japan. Geology 43, 151–154.
Van Westernen, W., Allan, N.L., Blundy, J.D., Purton, J.A., Wood, B.J., 2000. Atomistic simulation of trace element incorporation into garnets—comparison with experimental garnet–melt partition data. Geoch. Cosmoch. Acta 64, 1629–1639.
Veyland, A., Dupont, L., Rimbault, J., Pierrard, J.-C., Aplincourt, M., 2000. Aqueous chemistry of zirconium (IV) in carbonate media. Helv. Chim. Acta 80, 414–427.
Wang, S., Li, X.P., Duan, W., Kong, F., Wang, Z., 2019. Record of early-stage rodingitization from the purang ophiolite complex, western Tibet. Int. J. Earth Sci. 30 (6), 1108–1124.
Whitney, P.R., Olmsted, J.F., 1998. Rare earth element metasomatism in hydrothermal systems: the willsboro-Lewis wollastonite ores, New York, USA. Geochim. Cosmochim. Acta 62, 2965–2977.